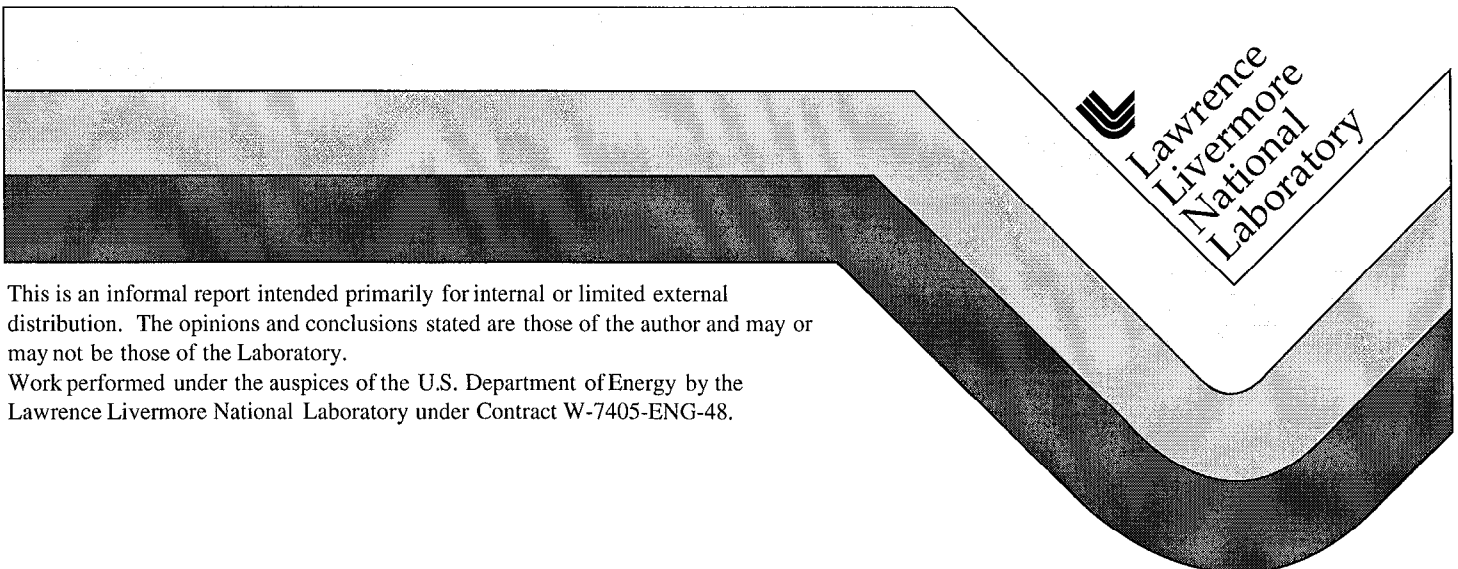# Short-Pulse Laser Materials Processing
1998 ERD-068 LDRL Final Report

P. S. Banks
M. D. Feit
A. Komashko
M. D. Perry
A. M. Rubenchik
M. Shirk
B. C. Stuart

April 2, 1999

Short-pulse laser materials processing

1998 ERD-068 LDRD final report

REVIEW COPY

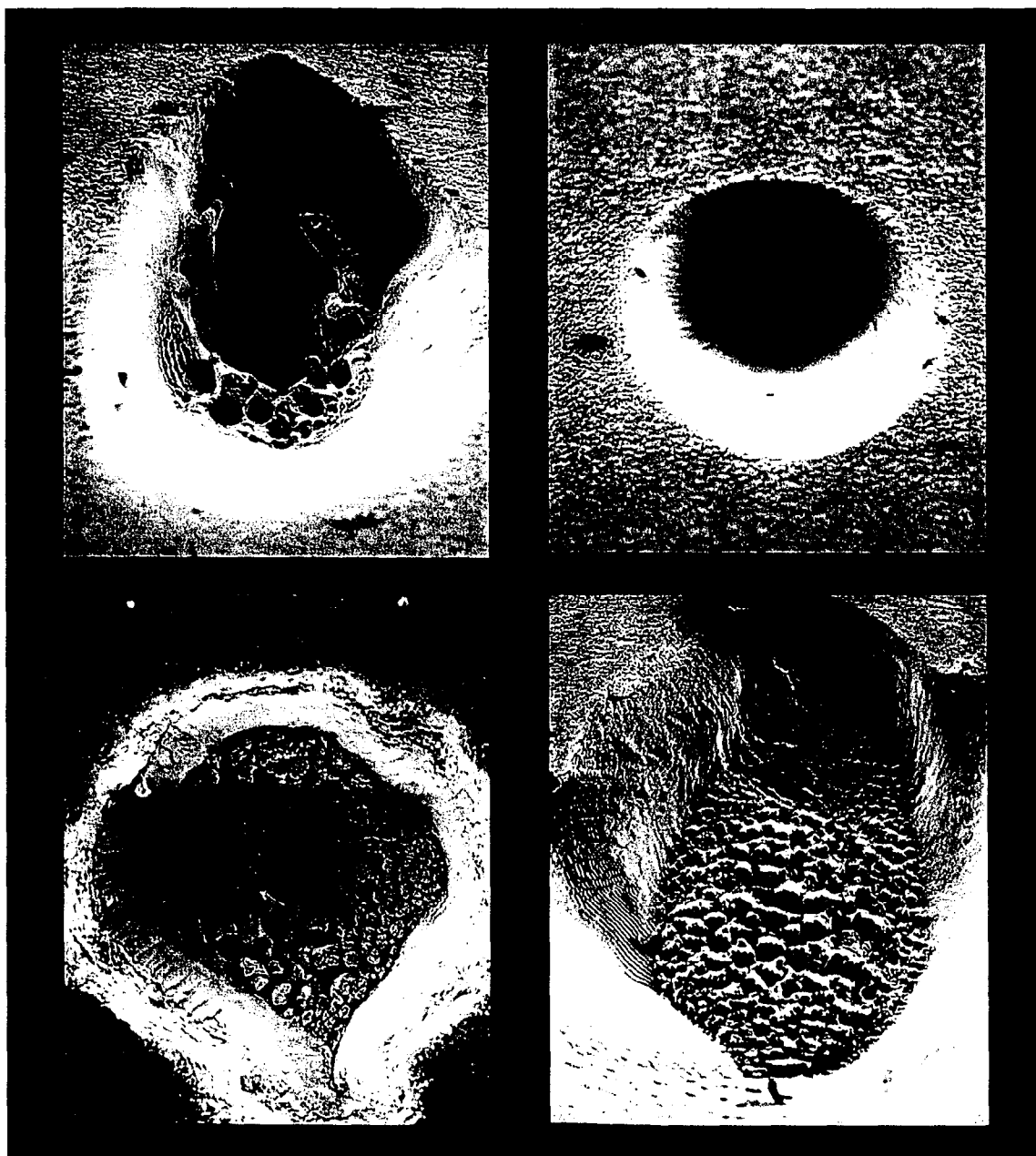P.S. Banks, M.D. Feit, A. Komashko, M.D. Perry, A.M. Rubenchik, M. Shirk, B.C. Stuart

Table of Contents

1. Introduction

The goal of this project was to develop, through experiments and modeling, a better understanding of the physics issues and machining techniques related to short-pulse laser materials processing.

We have shown over the past few years a new laser-based machining technology that utilizes ultrashort-pulse (0.1–0.4 picosecond) lasers to cut materials with negligible generation of heat or shock [1-7]. The ultrashort pulse laser has numerous applications in operations requiring high precision machining. Due to the extremely short duration of the laser pulse, material removal occurs by a different physical mechanism than in conventional machining. As a result, any material (e.g., hardened steel, ceramics, diamond, silicon, etc) can be machined with minimal heat- affected zone or damage to the remaining material.
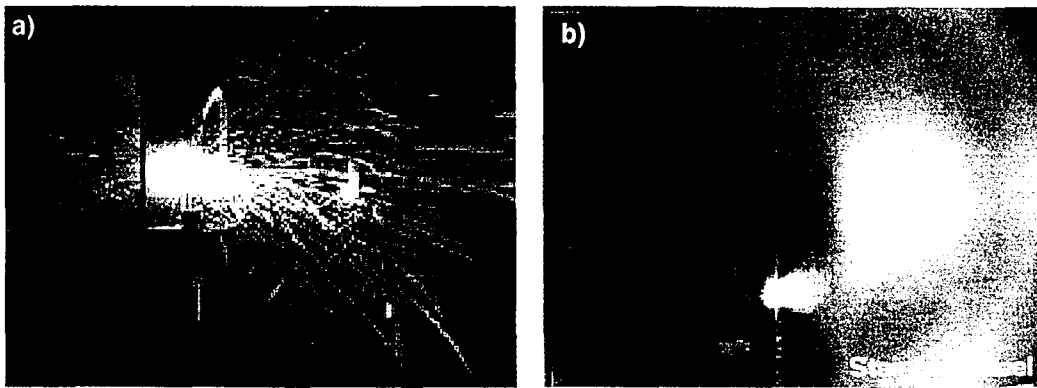
Figure 1.1. Machining of stainless steel with (a) conventional lasers and (b) with ultrashort (10^{-13} s) pulse lasers.

Conventional laser tools used for cutting or high-precision machining (e.g., sculpting, drilling) use long laser pulses (10^{-8} s to over 1 s) to remove material by heating it to the melting or boiling point (Fig. 1.1(a)). This often results in significant damage to the remaining material and produces considerable slag (Fig. 1.2(a)). With ultrashort laser pulses, material is removed by ionizing the material (Fig. 1.1(b)). The ionized plasma expands away from the surface too quickly for significant energy transfer to the remaining material. This different mechanism produces extremely precise and clean-edged holes or slots without melting or degrading the remaining material (Fig. 1.2(b)). Since only a very small amount of material (≈ 0.5 μm) is removed per laser pulse, extremely precise

machining can be achieved. High machining speed is achieved by operating the lasers at repetition rates up to 10 kHz or higher.
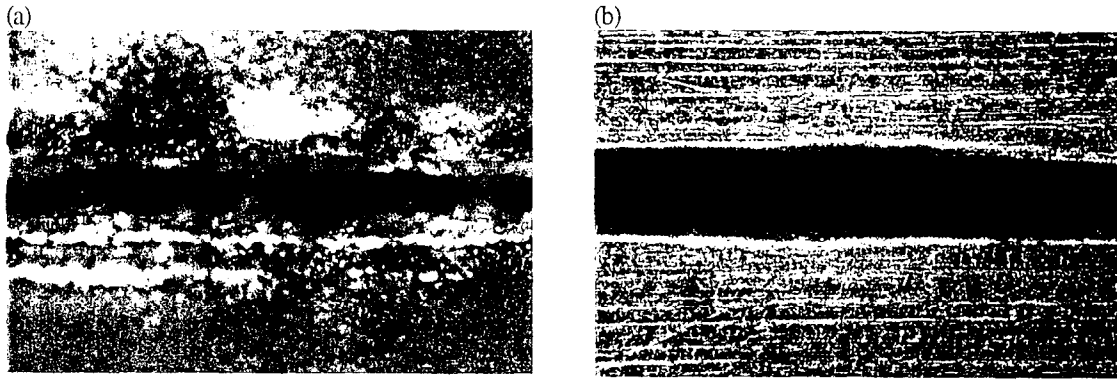
Fig. 1.2 Slots cut in 1-mm thick aluminum (a) with 1 ns pulses resulting in melting and slag, and (b) with 300 fs pulses producing a clean-edge cut.

Although we have successfully demonstrated many types of cuts in a wide range of materials, our general short-pulse machining scientific knowledge and our ability to model the complex physical processes involved are limited. During this past year we made good progress in addressing some of these issues, but as will be seen throughout this report there remain many unanswered questions.

Section 2 begins with a theoretical look at short-pulse laser ablation of material using a 1-D radiation-hydrodynamic code which includes a self-consistent description of laser absorption and reflection from an expanding plasma. In Section 3 we present measurements of scaling relationships, hole drilling progression, electric field and polarization effects, and a detailed look at the interesting structures formed during hole drilling of metals under various conditions. Section 4 describes the consequences of the presence of a prepulse before the main drilling pulse. In Section 5 we take a brief look at the plasma plume: how it can be useful, and how we can avoid it. Finally, Section 6 contains a couple of examples of machining non-metals.

The laser system used for practically all the experimental results presented here was a short-pulse laser based on Ti:sapphire, which produced 150-fs pulses (minimum) centered at 825 nm, of energy up to 5 mJ at 1 kHz, or 5 W average power.

2. Modeling of laser energy absorption and material removal in initially cold material

In the ultrashort pulse regime we are interested in, the initial hydrodynamic motion resulting from laser energy absorption is typically well described one-dimensionally because the energy is deposited in a thin pancake shaped region. The width of the pancake is determined by the beam size and the thickness is of the order of a skin depth (tens of nanometers). Thus, the simplest model of laser energy absorption is simply to declare that a certain fraction of the incident laser energy is deposited in a thin surface layer. This is sufficient for determination of some trends and regularities, but is, at best, only semi-quantitative. Despite the one-dimensional nature of the resulting hydrodynamics, the laser-material interaction depends strongly on the polarization of the laser light and its angle of incidence.

The next level of sophistication takes into account the index of refraction and absorption coefficient of the cold material to calculate Fresnel reflection and transmission coefficients. This gives explicit dependence on polarization and angle of incidence, but is still inadequate, in general, to treat quantitatively the laser energy absorption. The reason is that as laser energy is absorbed, plasma formation and expansion begin. Plasma expansion changes both the values of and the spatial distribution of refractive index, which in turn modifies the absorption during later parts of the pulse. Even for ultrashort pulses of less than one ps duration, plasma expansion can significantly affect the total pulse absorption as is shown below. Self-consistency is even more important in understanding the effect of prepulses, which create a pre-existent plasma profile for the main pulse.

Thus, a self-consistent description involving both vector electromagnetic wave propagation and plasma hydrodynamics is necessary for reliable description of laser energy deposition. We have implemented such a description in the hydrocode HYADES [8]. The incoming laser beam is propagated as a vector electromagnetic wave through a stratified (i.e. one-dimensional) plasma profile.

Below, we first describe the numerical method used to propagate the electromagnetic field and show typical generic results with fixed electron density profiles. We then present results from the integrated self-consistent optical propagation hydrodynamic modeling for ultrashort laser pulse interaction with Al.

3

It is intrinsically difficult to estimate theoretically the amount of material removal resulting from laser energy absorption. This is due to two reasons. Fundamentally, the initial density of deposited laser energy is extremely high. Response of the material involves hydrodynamic motion, shockwave generation and propagation, heat conduction, etc. Codes that describe these processes treat the material as a fluid. There is no model of material strength, fracture of cold material, etc. built into such fluid models. Second, detailed simulations model a relatively short time during and following the laser-material interaction. Actual material removal occurs on longer time scales after the material cools down and phase transformations and fracture occur. For ultrashort pulses (less than 1 ps, say), we can carry our simulations out to hundreds of ns, but it is inadvisable to push such modeling too far. In addition to the fact that the model becomes less useful for cold materials at low pressures, three-dimensional effects eventually become important. Thus, it is necessary to develop a short-time theoretical criterion correlated with material removal. As described below, we use the "long-time" zero velocity point to divide ablated from nonablated material. These simulations refer to the original material removal. At a later stage when holes of high aspect ratio are formed, considerations of waveguiding, wall absorption, and surface instabilities must also be taken into account.

2.1. Optical propagation model

We present here a simple numerical scheme for treating a medium with complex dielectric which varies only in the z direction. A plane wave is incident on this medium with arbitrary angle of incidence and polarization of either S (TE) or P (TM). The TE and TM notation is more useful since it reflects the nature of the electromagnetic wave, but the S/P notation is more generally used by experimentalists.

The basic idea is to treat the medium as a multi-layer, each layer having a constant complex dielectric constant. Consideration of the boundary conditions at an interface then, in an obvious generalization of the derivation of the usual Fresnel coefficients, leads to a linear relationship between the fields in one layer to the next. That is, they are connected by a 2x2 matrix. The overall properties (transmission and reflection) of the medium are found by multiplying all these matrices together. The fields penetrating the medium and the resultant energy deposition (Joule heating) can then be calculated. The advantage of this approach is its arithmetical simplicity - it is ideally suited for numerical computation since it involves many simple operations. By treating the field this way, we ignore the fact that the TM wave is non-transverse, i.e. we ignore the local contribution of $\nabla \cdot (E) = -E \cdot \nabla(\ln \varepsilon)$.

4

2.1.1 Formalism

We start by considering the fields at a planar interface between two media (1 and 2) with complex refractive indices n_1 and n_2, respectively (Fig. 2.1). The wave is incident from medium 1 at angle of incidence θ_1 as shown below and refracts at angle θ_2. In general, there are forward and backward waves in both media, we denote the forward going waves E or H with + and the backward waves E or H with -. The z-axis is normal to the interface, the y-axis normal to the figure.
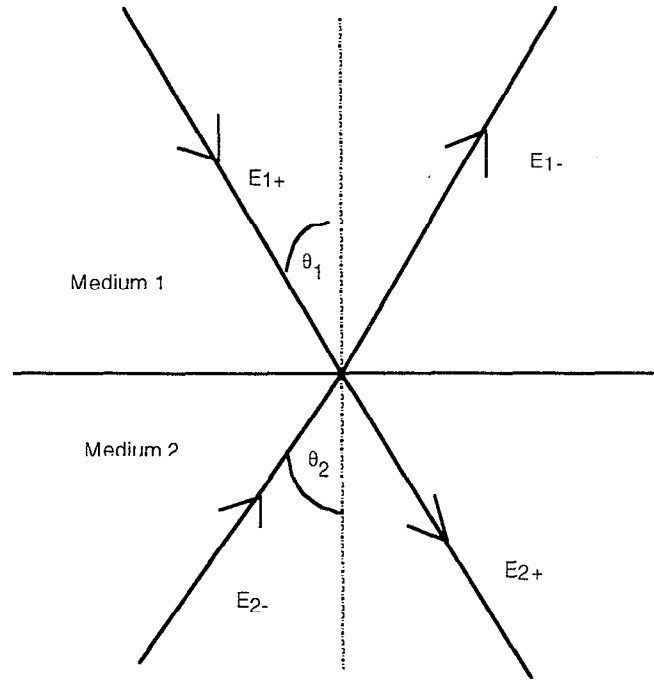

Fig. 2.1. Wave and media definitions.

Consider the two polarization cases separately. The boundary conditions are the continuity of E_x and H_y for the TM case and of H_x and E_y for the TE case. This gives:

for S polarization,

$$E_{1+} + E_{1-} = E_{2+} + E_{2-}$$
$$\cos(\theta_1)\, n_1(E_{1+} - E_{1-}) = \cos(\theta_2)\, n_2(E_{2+} - E_{2-})$$

(2.1)

5

and for P polarization,

$$H_{1+} + H_{1-} = H_{2+} + H_{2-}$$

$$\frac{\cos(\theta_1)}{n_1}(H_{1+} - H_{1-}) = \frac{\cos(\theta_2)}{n_2}(H_{2+} - H_{2-})$$

(2.2)

In either case, the fields on each side of the interface are connected by linear equations of form,

$$\begin{pmatrix} F_{2+} \\ F_{2-} \end{pmatrix} = M_{2,1} \begin{pmatrix} F_{1+} \\ F_{1-} \end{pmatrix}$$

(2.3)

If medium 2 has a finite thickness w_2, the fields at the end of this layer are connected to the above matrix by another 2x2 (diagonal) matrix P whose diagonal elements are $Exp[\pm\, i\, k_{z2}\, w_2]$, where k_z is the (complex) longitudinal wavenumber (note that transverse wavenumber is fixed by Snell's law as $k_x = k_0\, \sin(\theta_0)$), i.e.,

$$(k_z/k_0)^2 = \varepsilon - \sin^2(\theta_0).$$

(2.4)

Thus, the product of two matrices of this type propagates the fields from the entrance of one layer to the entrance of the next layer. In this way we can work through the entire medium.

Analyzing the above product matrix for N layers, one can determine net reflection r, and transmission t, amplitudes. One can stop when the transmission is as small as desired for a metallic (absorbing) medium. The net flux along the z-axis into the medium is given by $\cos(\theta_0)$ $(1-|r|^2)$, which is balanced by the flux absorbed or transmitted in the medium. The energy absorption rate is given by the electrical conductivity times the square of the electric field. In terms used here, we use the energy deposition density, $Im[\varepsilon]\, |E|^2\, k_0$.

2.1.2 Static Examples

Consider a laser beam incident at 45° with S-polarization onto a plasma whose density rises linearly with z to twice the critical density ($n_c=10^{21}$ cm^{-3} for 1 μm light) over a half wavelength distance. We use a Drude dielectric formulation for the plasma with a scattering time τ such that $\omega\tau=10$, with ω being the laser radian frequency. Figure 2.2(a)

6

shows the calculated value of $|E|^2$ in the medium, which drops off exponentially with penetration as expected. Energy absorption is proportional to $Im(\varepsilon)$ $|E|^2$ which is plotted in Fig. 2.2(b) and seen to peak just inside the surface. The cumulative absorption is shown in Fig. 2.2(c).

Fig. 2.2(a) Square of S-polarized field penetrating metal vs. depth z (units of wavelength). Angle of incidence is 45°.

Fig. 2.2(b) Density of laser energy absorption corresponding to Fig. 2.2(a)

Fig. 2.2(c) Laser energy absorbed up to depth z corresponding to Fig. 2.2(a). S-polarization.

The importance of polarization is evident in comparing the corresponding results for P-polarization shown in Figs. 2.3(a)-(c). In this case, resonance absorption occurs at the critical electron density. This results in higher and more localized energy absorption, as seen in Fig. 2.3(b). This result is completely analogous to the peak in absorption seen for P-polarization at high angles of incidence on metals.
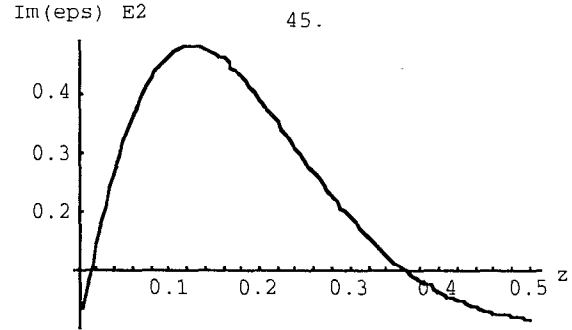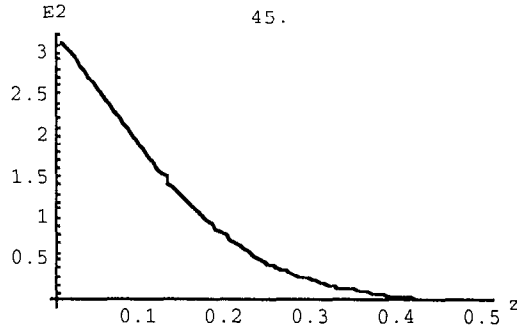
7
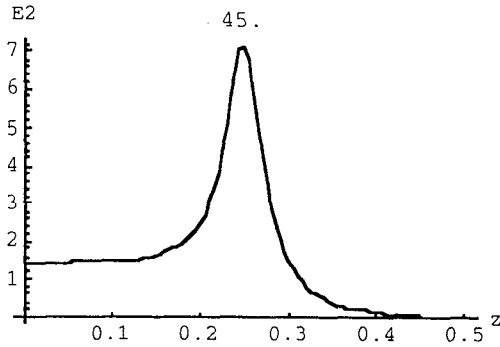
Fig. 2.3(a). Square of P-polarized field penetrating into metal vs. depth z (units of wavelength). Angle of incidence is 45°.
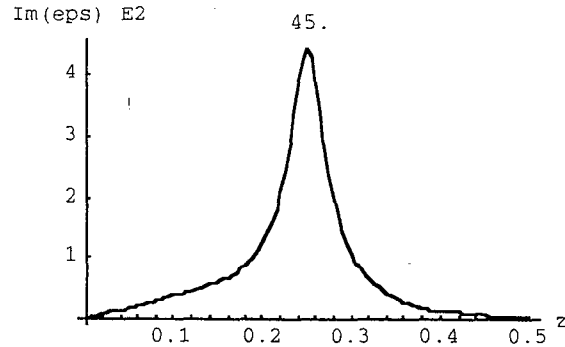
Fig. 2.3(b). Density of laser energy absorption for P-polarization corresponding to Fig. 2.3(a)
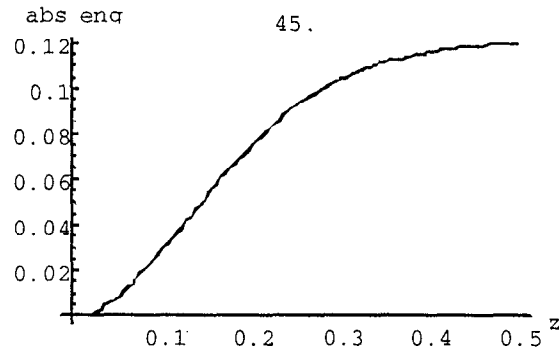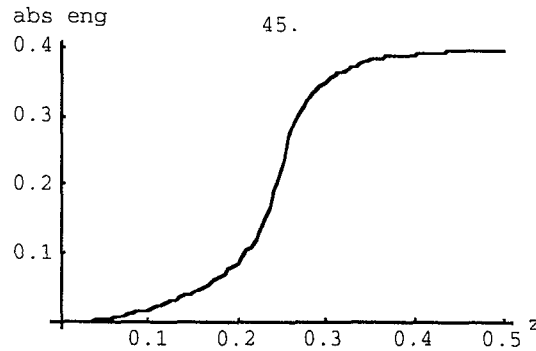

Fig. 2.3(c). Laser energy absorbed up to depth z corresponding to Fig. 2.3(a). P-polarization.

2.1.3 Results of integrated laser absorption - hydrodynamic modeling

The examples shown below refer to aluminum since a reliable equation of state suitable for the laser-ablation regime was available. Consider a 150 fs, 16 J/cm^2, 825 nm, P-polarized laser pulse incident on Al. Carrying out the self-consistent calculation described schematically above, results in the electron concentration and energy deposition profiles shown in Fig. 2.4 at the time of peak intensity. Note the depth scale is in nm and that the peak energy deposition is not at the peak electron density. These distributions evolve with time. For example, at 700 ps after the peak of the laser pulse, the temperature and density profiles with depth are as shown in Fig. 2.5. Note the compression of Al behind the shockwave, which has propagated to about 5 μm in 1 ns. Also, high temperatures exist mostly in the blow-off plasma; shock heating of the solid is a few hundred degrees near the surface.
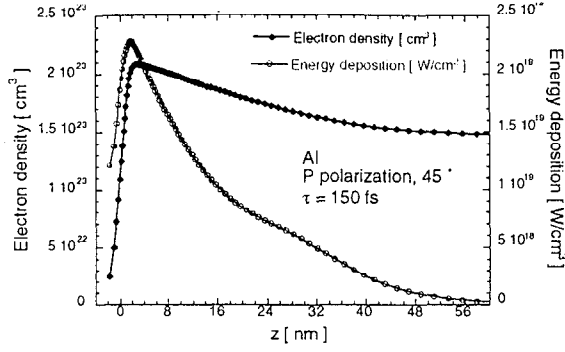
Fig. 2.4. Electron density profile and energy deposition vs. depth at peak of 150 fs, 16 J/cm² pulse on Al. Initial solid is on positive depth axis.
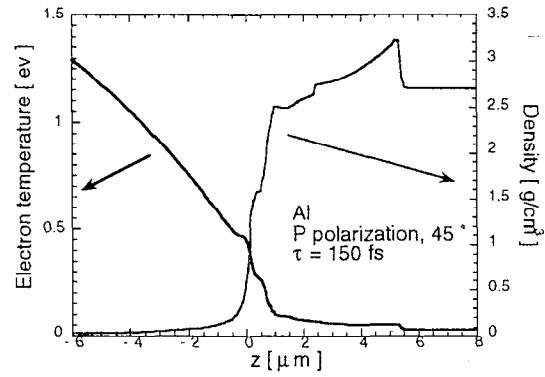
Fig. 2.5. Mass density and electron temperature profiles 700 ps after time of Fig. 2.4.

If one holds the pulse duration fixed at 150 fs and varies the intensity, the absorption begins to rise for fluences greater than about 1 J/cm² due to the high-density "cold" plasma distribution as described earlier (Sec.2.1.2). At very high fluence, however, the plasma becomes hot enough that inverse-Bremstrahlung absorption drops. This effect is shown in Fig. 2.6. It is instructive to look at the net absorption at low and moderate fluence as a function of angle of incidence (Fig. 2.7). Absorption expected from the Fresnel coefficients calculated from the optical properties of cold Al are also plotted in the figure. It is seen that the low fluence (1.6 J/cm²) pulse has absorption substantially the same as one expects from the cold material. However, at a fluence of 16 J/cm², absorption is found to increase considerably at all angles of incidence and for both polarizations. We carried out a similar numerical experiment for carbon. In this case, the cold absorption is high to begin with and the effect shown in Fig. 2.7 is not so dramatic.
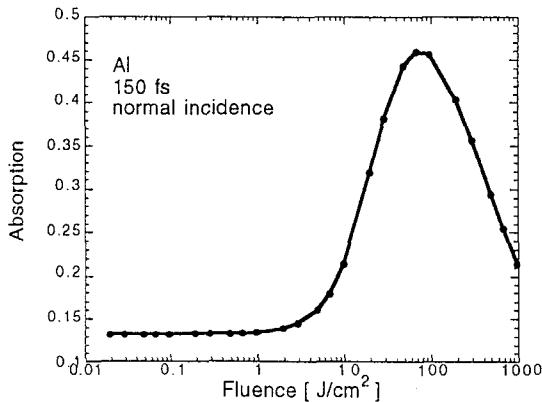
Fig. 2.6. Fraction of normal incidence, 150 fs laser pulse absorbed by Al as function of pulse energy fluence.
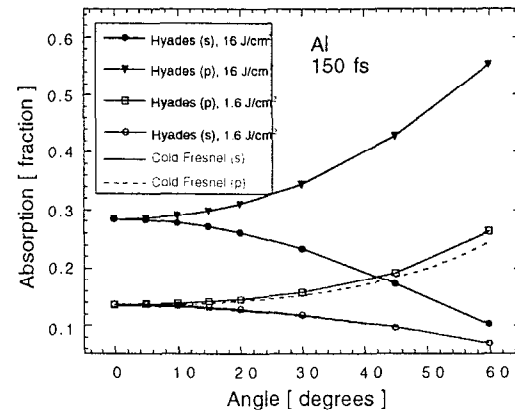
Fig. 2.7. Net absorption of low fluence laser pulses can be estimated from cold Fresnel reflection and transmission coefficients. This is modified at high fluence through interaction of the pulse with plasma.

9

2.2. Material removal

We used two short time estimators of ultimate material removal by laser ablation of a pristine surface. The first is the very natural approach of measuring the mass flow through a plane just outside the original material surface. While this yields a measure related to ultimate removal, the limited time over which the integration can be carried out results in absolute numbers that strongly underestimate actual values. We found a better estimator to be given by locating the point at which zero material velocity occurs at times many pulselengths after the laser-material interaction. The idea is that all mass on one side of this point will leave the solid while that on the other represents the solid material motion leading to compression. Figure 2.8 shows the computed mass density as a function of time and space for a 1.6 J/cm^2, 150 fs pulse incident on Al. This evolution is followed for one ns. The spatial coordinate here is the Lagrangian coordinate fixed in a mass element. The laser energy absorption occurs on a time scale too short to be evident in this depiction. One sees a shockwave launched into the solid material (top) compressing the Al behind it. During the same period, the outermost zones blow off as rarefied vapor. Superposed on the

Fig. 2.8. Mass density evolution following irradiation of Al with 150 fs, 1.6 J/cm^2 pulse. Long-time position of zero-velocity contour (green line) is used to estimate amount of ultimate material removal.

10

color figure are temperature and velocity contours. The solid red contour corresponds to the melting temperature, while the dashed red contour corresponds to the boiling temperature under normal conditions. The green contour corresponds to zero velocity. All mass below this contour is moving away from the solid. Note that the Lagrangian position of the zero velocity contour becomes 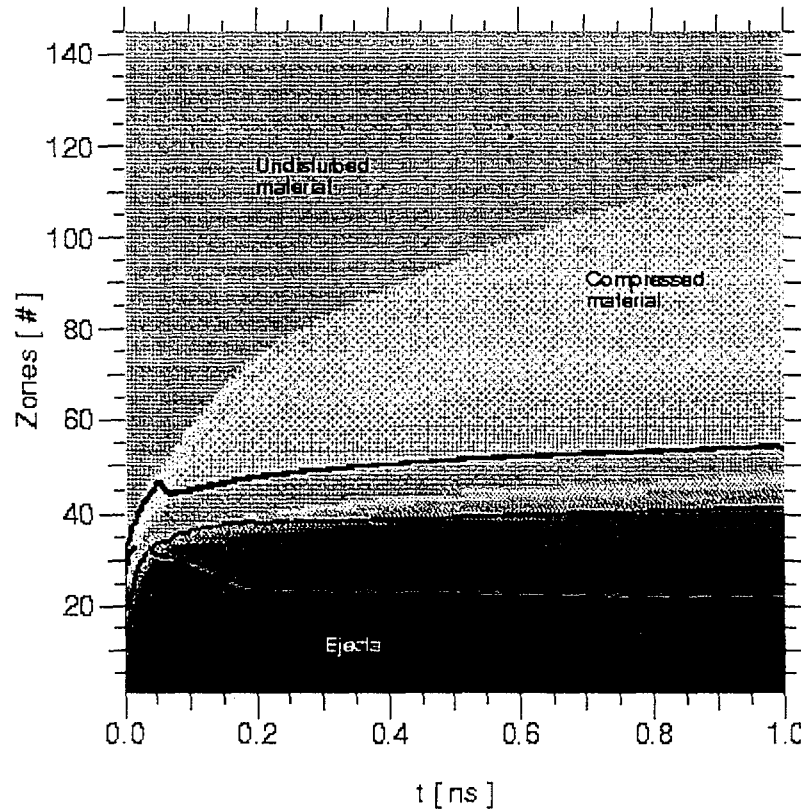relatively constant a short time after the laser interaction. In the following, we use this contour to estimate mass removal via ablation. Note that this estimation neglects the effect of long-time evaporation. This is most appropriate for metals because they cool rapidly.

2.2.1 Energy Efficiency

We used the zero-velocity criterion to carry out several systematic investigations of the energy efficiency of material removal with short laser pulses. Figure 2.9 illustrates the transition from ultrashort to longer pulse ablation behavior. Here, the total energy absorption and material removed are calculated as a function of pulse width for a fixed energy fluence of 1.6 J/cm^2. Note that there is almost no dependence of either quantity on pulsewidth for pulses shorter than about 1 ps. For such short pulses, energy deposition is effectively instantaneous (thermal diffusion length and hydrodynamic expansion are small compared to the skin depth). For longer pulses, the total absorption increases. However, most of this increase in absorption takes place in the expanding plasma, which is further removed from the solid surface. A much higher proportion of absorbed energy ends up as waste heat in the plasma in the case of longer pulse durations.

We also examined theoretically the material removal rate as a function of fluence at fixed pulse duration of 150 fs (Fig. 2.10). Although the amount of material removed per pulse increases with incident fluence, the fluence specific removal rate (depth removed per unit incident fluence) is calculated to be maximal just before the onset of appreciable material removal (see Fig. 2.10). This point is not necessarily an optimal operating point for material processing, however, since it implies very many more pulses are necessary for a given amount of material removal than would be required at a higher, less energy efficient, incident fluence.
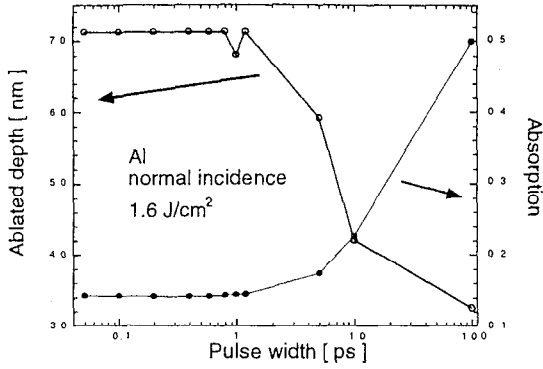
Fig. 2.9. Dependence of laser energy absorption and material removal on pulse width at constant fluence (1.6 J/cm^2).
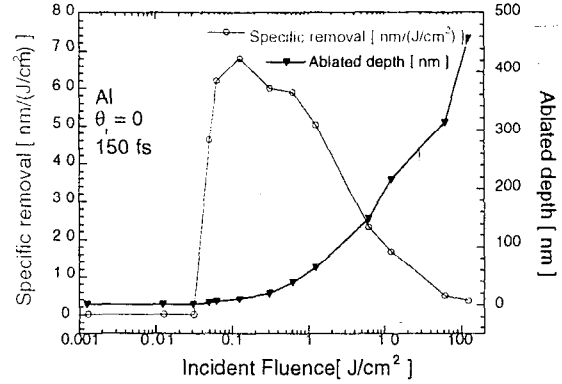
Fig. 2.10. Ablated depth and fluence specific initial material removal as a function of incident fluence for 150 fs pulse on Al. The most energy efficient removal occurs at low fluences of about 0.1 J/cm^2.

2.2.2 Prepulse

From the absorption results presented above, it is evident that for P-polarization the usual inverse-Bremstrahlung absorption can be supplemented and increased by resonance absorption provided a plasma of the right scale length (fraction of a wavelength) is available. This suggests that material removal might be optimized by using a prepulse to create a plasma profile for the main pulse. An optimum is expected with respect to timing between the prepulse and main pulse since if the temporal separation is too long, laser energy is absorbed in the plasma far away from the solid and does not contribute to additional material removal. Our detailed calculations bear out this simple idea.

An example of such a calculation for a 100 fs pulse incident on Al is shown in Fig. 2.11. Here a 10% prepulse arrives at the time marked by the first arrow and the main pulse arrives at the time of the second arrow. Pressure evolution in space and time is shown with the solid initially occupying the positive z-axis. The laser beams arrive from the top. Note that two shock waves are generated. The weaker shock due to the prepulse is eventually overtaken by the stronger shock launched by the main pulse.

Laser energy absorption depends on both laser intensity and the lag between the main and pre-pulses. Figure 2.12(a) shows the breakdown between inverse-Bremstrahlung and resonance absorption for a 150 fs, 10^{13} W/cm^2 main pulse with a 10% prepulse. A broad peak in absorbed energy is noted. Figure 2.12(b) shows corresponding quantities for a pulse with 10 times the intensity and a 5% prepulse. However, *absorption does not correspond directly to material removal*, as noted above. The calculated material removal

12

rate corresponding to conditions of Fig. 2.12(a) is given in Fig. 2.13, where a definite optimum removal rate is seen at 20 ps separation.

While this result is correct, it unfortunately does not reveal how to optimize practical large-scale material removal such as hole drilling. The reason is that after the hole begins to form, the walls of the hole are at different angles to the incident beam direction and polarization than the angles of the original surface. Electric currents are generated in the walls and act as a laser energy sink and heat source. The loss of laser energy to the walls can be significant. Also, surface instabilities (corrugations) form which futher modify the interaction of the laser beam with the solid material. With corrugations, the angle of incidence varies with position. In this case, there is not necessarily an optimal prepulse timing and the presence of prepulses can result in a reduction in the amount of material removed. We have not fully addressed all these issues during the limited time of this project.
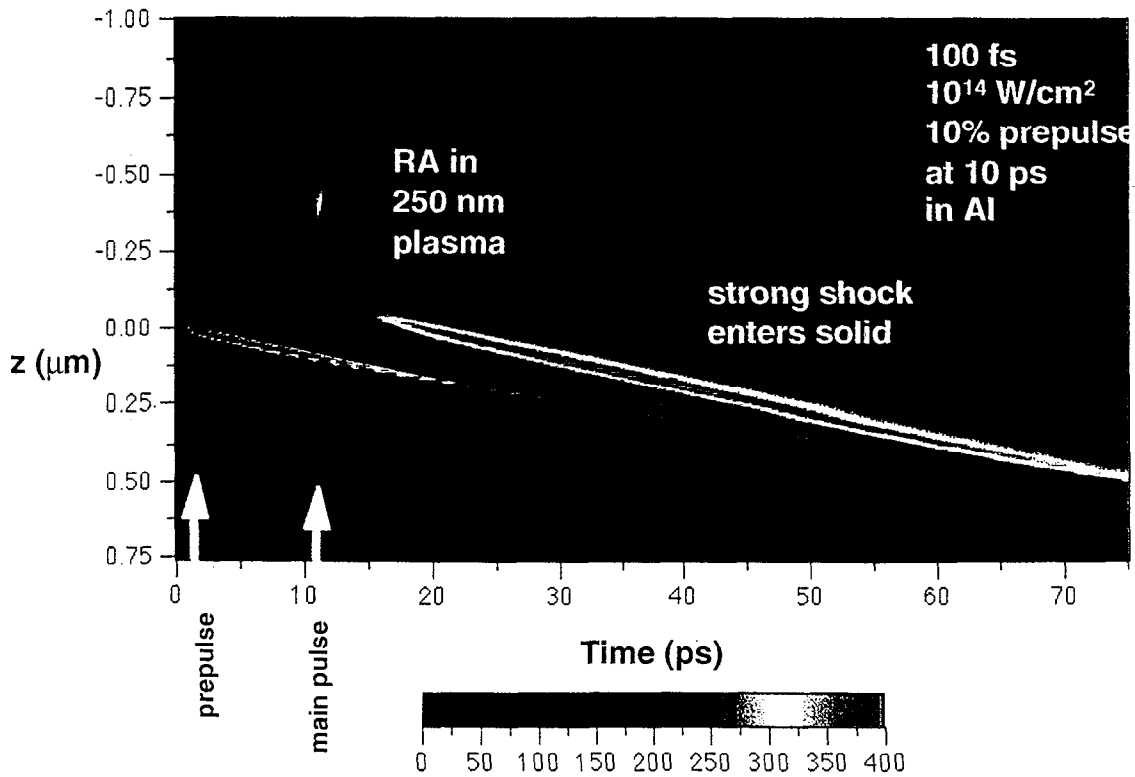
Fig. 2.11. Pressure evolution in space and time accompanying resonance absorption (RA) of the main laser pulse in a prepulse-generated plasma profile.

13
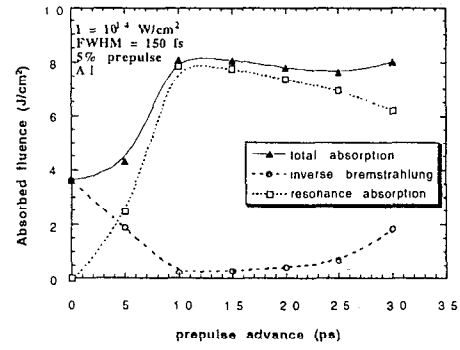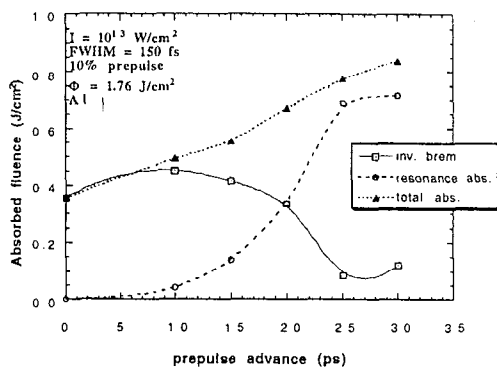
Fig. 2.12. Decrease of inverse-Bremstrahlung and increase of resonance absorption due to prepulse-generated plasma profile. (a): 10^{13} W/cm^2, 10% prepulse,

(b) 10^{14} W/cm^2, 5% prepulse. Note broad energy absorption peak.
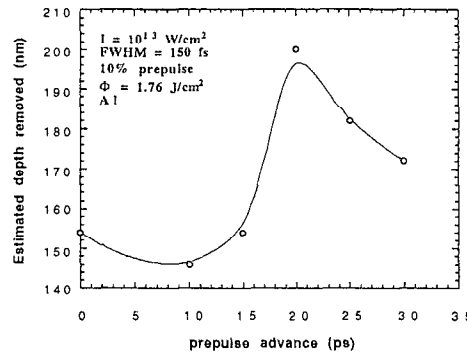
Fig. 2.13. Material removal rate calculated for conditions of Fig. 2.12(a) as function of temporal separation of main and prepulse. At optimal prepulse timing, material removal is increased by 33%.

2.3 Surface relief on metals

Plane metal surfaces irradiated by laser light can be unstable to growth of surface relief patterns. The instability can be explained as follows (see e.g. review [9]). Let us consider a small periodic modulation (grating) of the surface with wave number g. The surface modulation diffracts the incident wave. The interference of incident and diffracted waves produces a periodic modulation of light absorption. If this modulation of absorption causes grating growth, we have a feedback mechanism driving the surface modulation.

14

The problem of surface relief excitation was treated previously mainly for long laser pulses, where a few mechanisms of feedback were investigated [9]. First, the evaporation mechanism must be mentioned. Higher local intensity increases the surface temperature and enhances evaporation producing relief growth. Also the thermocapillary mechanism and melt motion under the effect of vapor reciprocal momentum were considered. All these mechanisms are irrelevant to ultrashort-pulse laser interaction with metals. In our case, material removal is determined by the local fluence. Interference of the incident and scattered waves results in fluence modulation and produces feedback for relief growth. For long pulses, instability development takes place during the pulse. For ultrashort-pulse laser the melt thickness and cooling time are small and removal modulation survives up to the next shot. Relief formation takes place after many shots.

It is important to mention that the wavelength of most unstable relief patterns is insensitive to the feedback mechanism. It is evident that the interaction with the surface modulation will be most efficient if the scattered wave propagates along the surface, giving a surface electromagnetic wave. For this we must have,

$$k_t \pm g = k_s; |k_t| = k \sin \vartheta; |k_s| = k \qquad (2.5)$$

The maximal growth has structures in which the tangential part of the incident light electric field will be parallel to the vector $\mathbf{g}$. For p-polarization we have for the relief wavelength,

$$\lambda_s = \frac{\lambda}{1 \pm \sin \vartheta}. \qquad (2.6)$$

For 45° angle of incidence, the relief wavelength is about 3.4 laser wavelengths. For s-polarization,

$$\lambda_s = \frac{\lambda}{\cos \vartheta}, \qquad (2.7)$$

and the relief wavelength is 2.4 times shorter. From Fig. 4.3 one can see that both the orientation and relief wavelength are consistent with the above estimates.

Such periodic structures were observed only for low fluence regions, e.g. only on the laser spot edge. For high fluence we observed the smoothing of short scale corrugation and development of deep and long wavelength surface modulation. The smoothing is probably related to the change of the local heat of evaporation due to the curved surface,

$$L_{eff} = L - (\sigma / \rho)(1 / R_1 + 1 / R_2),$$
(2.8)

where L is the specific heat of evaporation for a plane boundary, σ is the surface energy density (surface tension) and R_1 and R_2 are the principal radii of boundary curvature. The development of long wavelength surface modulation is driven by the local change of absorption due to the local variation of polarization and angle of incidence.

2.4 Summary

We formulated a vector optical propagation scheme accounting for laser beam polarization and angle of incidence. This scheme has been implemented into the one-dimensional radiation-hydrodynamic code HYADES and permits a self-consistent description of laser absorption and reflection from an expanding plasma. This is important for quantitative modeling since laser pulse absorption can be quite different from that expected from the "cold" Fresnel coefficients. We also developed theoretical estimates of ultimate material removal due to ablation. Detailed calculations demonstrate the high energy efficiency of material removal using ultrashort laser pulses and aid in determining optimal operational parameters.

3. Cutting and drilling of metals

Numerous effects of the laser and material parameters were investigated to determine their influence on the rates and quality of short-pulse laser machining of metals.

3.1 Reflectivity effects

One of the most significant aspects of hole geometry to industrial customers is the hole taper, or the amount the hole diameter varies with depth. Fully understanding what processes affect the final hole taper is important in order to be able to meet the various requirements our customers have. It was suggested that the taper observed in the hole would be influenced by the reflectivity of the material, i.e. material with a higher reflectivity would absorb less, resulting in more energy making it to the bottom of the hole. This would mean more of the beam would be above threshold, leading to larger hole diameters at the exit, and thus to less taper. To test this, we drilled holes in 750 μm thick copper plate and 1.2 mm thick 304 stainless steel without any change in laser parameters: 2 J/cm^2, 350 μm flat top spot, 150 fs, 0° AOI, and circular polarization. The flat top spatial profile was formed by imaging an aperture which clipped the beam at approximately the 50% level.

The measured drilling rates were 30 nm/pulse for the stainless steel and 12 nm/pulse for the copper. These rates were measured by recording the amount of time required from initial ablation to first observation of light leaving the exit of the hole. This decrease in drilling rate is expected since copper has a much higher reflectivity for 820 nm light (96% at 0° AOI) than does steel (61% at 0° AOI). Less of the incident pulse energy is coupled into the copper. This is true to a lesser extent at near-grazing incidence on the walls once the hole is formed. In this case (~85° AOI), the reflectivity for copper is 99.8% for light polarized parallel to the wall and 93% for light polarized perpendicular to the wall while the reflectivity for stainless steel is 96% and 45%, respectively. An optical microscope was used to measure the diameter of the hole at several distances from the laser entrance surface with the results shown in Fig. 3.1. It is evident that the taper of the hole is essentially unchanged between copper and steel.
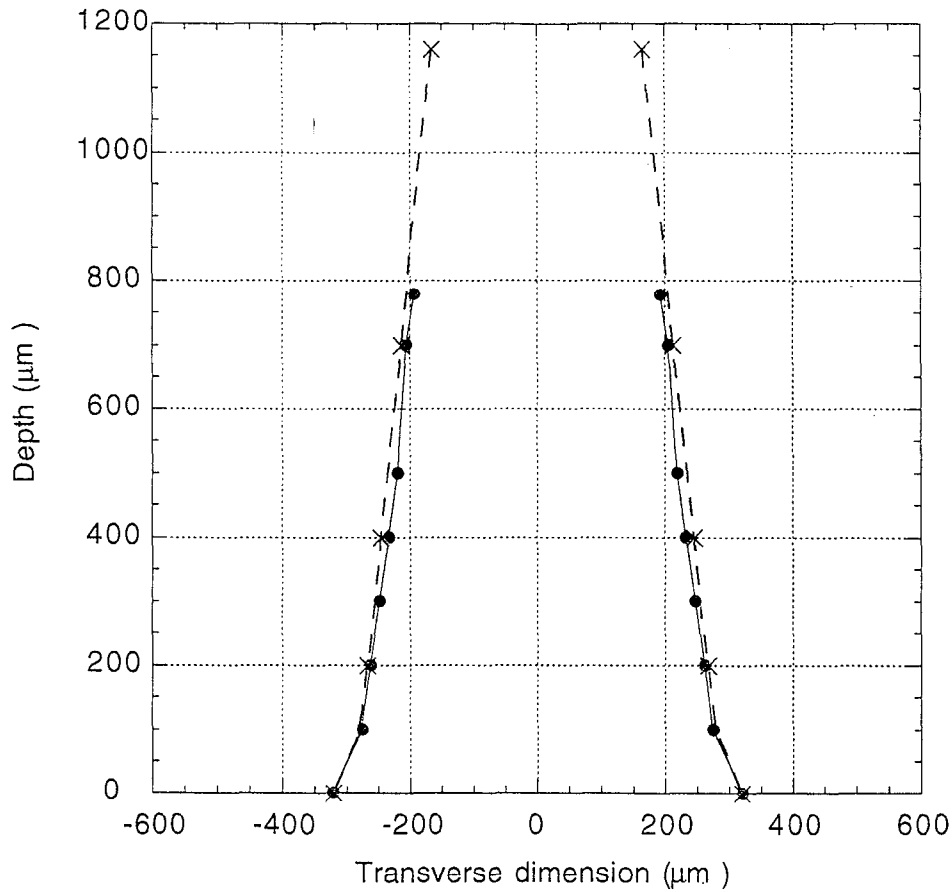
Fig. 3.1. Profile of hole drilled in copper (red dots/solid line) and 304 stainless steel (green x/dashed line) at 2 J/cm^2, 350 μm diameter top hat spot, 150 fs, and 0° AOI.

3.2 Redeposition of material

We did a brief examination of how material from the bottom of the hole is redeposited on the hole walls, i.e. how much of the material escapes. To accomplish this, holes were drilled in 750 μm stainless steel plates backed by a copper plate at 0° AOI. The laser was left on well after the breakthrough time for these laser conditions. The holes were examined using an optical microscope in an attempt to assess the amount of copper deposited on the hole walls. For holes drilled for more than 5 s beyond breakthrough, large (> 80 μm), irregular deposits of copper were observed up to 200 μm from the hole bottom.

An example of such a deposit is shown in Fig. 3.2. This hole was drilled with 5 J/cm^2 and a 300 μm spot for 10 s beyond the breakthrough time (15 s). A circle approximates the hole without the copper, and the material within this circle is mostly copper from the

18

second plate. There is currently no explanation as to how the nonuniform clumps could form without being ablated by the next pulse or series of pulses. It also appeared that the hole walls were coated with a thin layer of copper up to the hole entrance. It may prove possible to section these holes without contaminating the surface and determine the copper concentration spectroscopically as a function of depth.
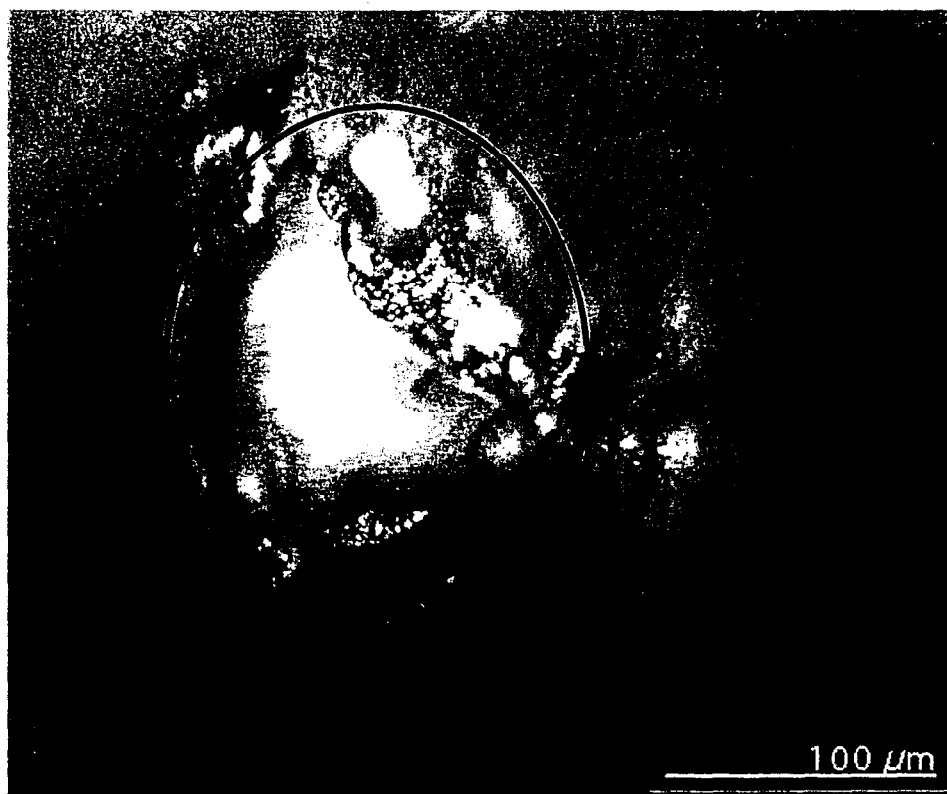
Fig. 3.2. Optical photomicrograph of copper deposits near (but not at) the bottom of a hole drilled in stainless steel. The circle approximates the hole as it would be with no copper present.

3.3 Progression of hole drilling

A series of holes was drilled under the same laser conditions (0.5 J/cm^2) while varying the number of shots used to form the holes from 5 to 20,000. The depths of the holes were measured and are shown in Fig. 3.3(a). The depths are accurate to within 2–3 μm so the depths measured for low number of shots have large error bars. However, after the first few hundred shots, the growth of the hole with time becomes nearly linear. In Fig. 3.3(b) the drilling rate along the hole axis is plotted. It can be seen that the initial drilling rate can

19

be quite high (~1 μm/pulse), but this quickly decreases to less than 100 nm/pulse and becomes nearly constant (and thus the near linear dependence of depth on the drill time). This happens within the first 100 μm or so of the hole. SEM photomicrographs of these 14 holes are shown in Fig. 3.4 as well, to illustrate the progression of the hole morphology with time.

(a)

(b)
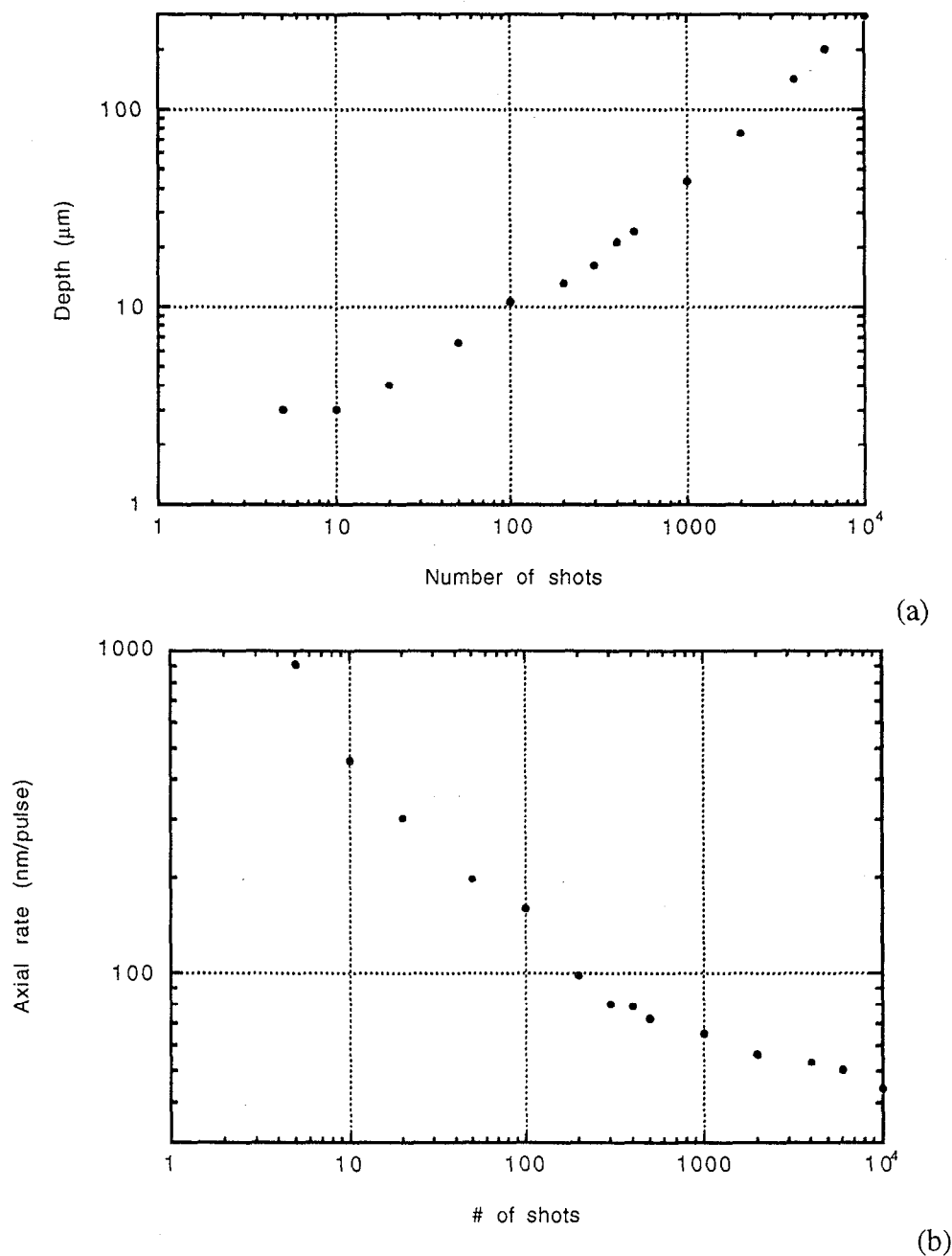
Fig. 3.3. (a) Hole depth, and (b) drilling rate as a function of number of shots with 0.5 J/cm^2, 60° AOI, circular polarization
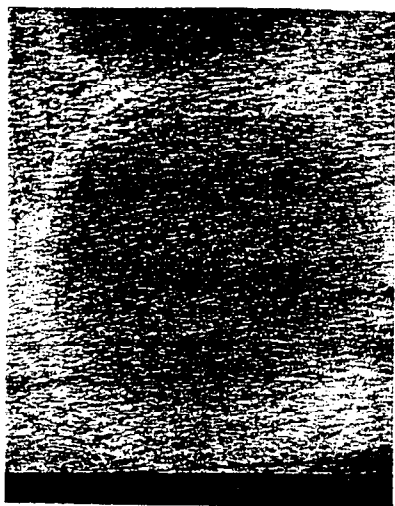
(a)

(b)

(c)
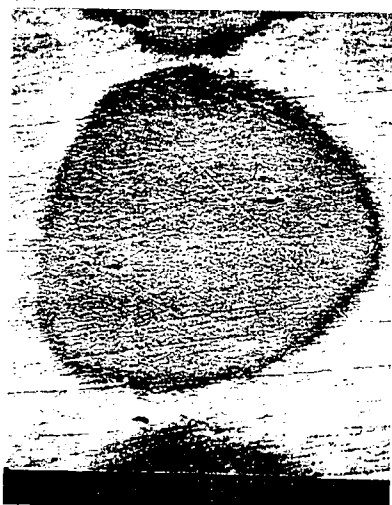
(d)
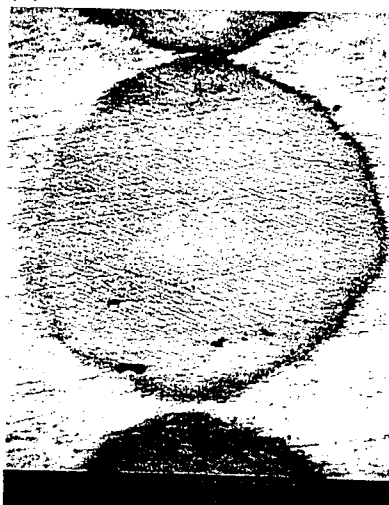
(e)
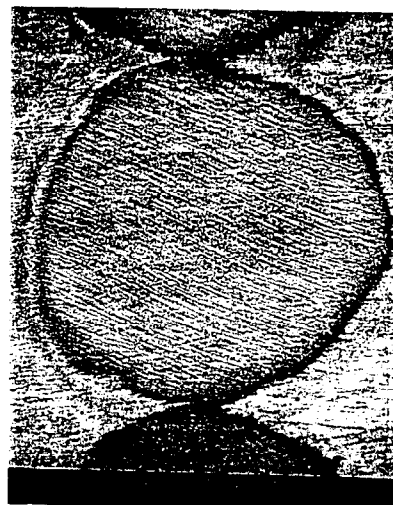
(f)
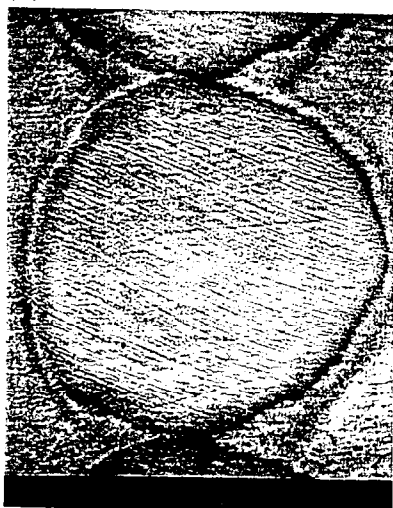
(g)
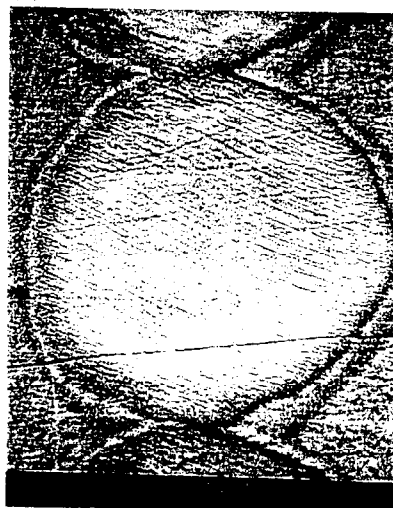
(h)
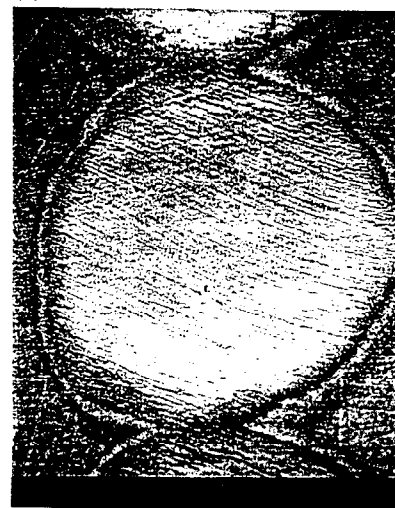
(i)
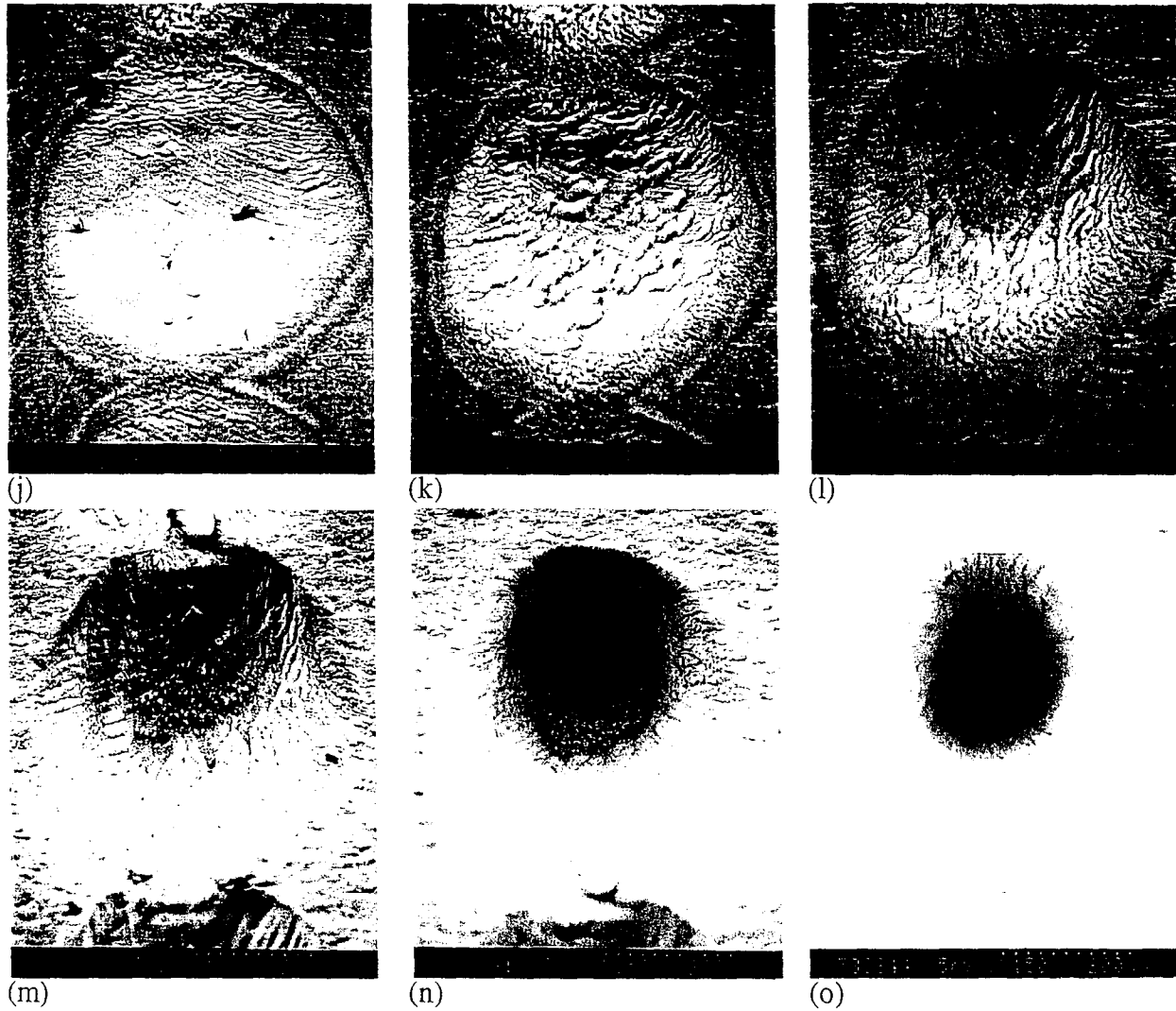
Fig. 3.4. SEM photomicrographs of holes drilled at 0.5 J/cm^2 and 60° AOI for (a) 5 shots, (b) 10 shots, (c) 20 shots, (d) 50 shots, (e) 100 shots, (f) 200 shots, (g) 300 shots, (h) 400 shots, (i) 500 shots, (j) 1000 shots, (k) 2000 shots, (l) 4000 shots, (m) 6000 shots, (n) 10000 shots, and (o) 20000 shots.

3.4 Structures formed during hole drilling

Figures 3.5-3.9 show SEM photomicrographs of holes drilled under various conditions which illustrate several of the interesting features which we have observed. Figure 3.5 shows a picture of a hole drilled with a quasi-flattop beam formed by imaging an aperture which clipped the beam at about the 50% level. The hole was drilled in a single-crystal alloy at 60° AOI and 0.3 J/cm^2 with circular polarization, and the laser was left on for 90 s (first breakthrough was detected at 45 s). There are pronounced grooves evident in the side walls of the hole, particularly toward the left in the picture. A higher magnification view of

22

Fig. 3.5. (a) SEM photomicrograph of hole drilled with imaged beam clipped on aperture at about the 50% level (fluence is 0.3 J/cm²). (b) higher magnification picture of the bottom wall near the surface. (c) higher magnification of the grooves along the left wall.

23

these grooves in the left wall is shown in Fig. 3.5(b). The grooves are remarkably regular and almost hemispherical in cross-section, and are 2–3 μm in diameter. However, a close-up view of the lower wall (Fig. 3.5(c)) shows only small undulations in the surface—there are no well defined grooves visible. Groove structures in the side walls of holes seem to be fairly common at low fluences.

Fig. 3.6 shows the morphology of a hole drilled in stainless steel for 5 s (5000 shots) at 60° AOI, P polarization, 1 J/cm², and 150 fs pulse. The same bottom roughness can be seen. In Fig. 3.6(b) a series of parallel grooves with a period of approximately 4 μm can be seen on the left side wall of the hole. These grooves are of a different nature than those seen in Fig. 3.5, and they do not appear in any other portion of the hole. However, as will be shown later, these parallel grooves are common to many of the holes drilled with P polarization. Fig. 3.6(c) shows the bottom wall from Fig. 3.6(a) at higher magnification, and a distinct texturing of the hole wall can be observed. The causes for these features are not known.

(a)   (b)
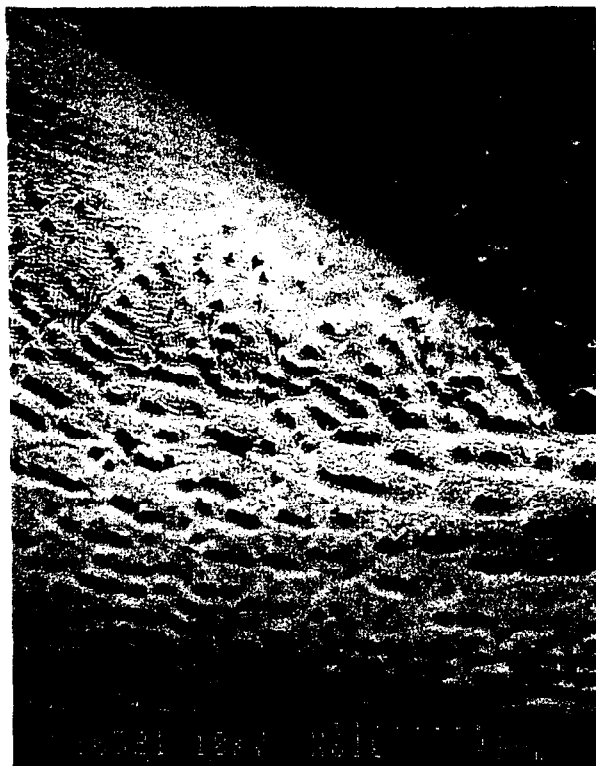
(c)

Fig. 3.6. SEM photomicrograph of hole drilled in stainless steel using a 600 μm spot and P-polarization at 1 J/cm² and 60° AOI for 5000 shots. The plane of incidence is vertical in the page.

The hole in Fig. 3.6 was drilled using a 600 μm diameter spot. The spot size was reduced to 350 μm while maintaining constant fluence and another hole was drilled for 5000 shots and is shown in Fig. 3.7. Grooves similar to those seen in Fig. 3.6(b) are again evident on both sides of the hole although the period does not appear to be constant. In fact, as the grooves move to the underside of the hole, the period reduces to approximately 1 μm. On this side, there are also grooves which are perpendicular to the grooves mentioned above with a period of about 2 μm, as well as deeper, quasi-periodic crevices towards the left side of the underside. Finally, nearly perfect circular holes can be seen ranging in diameter from 1 μm to 15 μm. Again, we have no explanations for the causes of these features, but they are similar in appearance to geologic features due to volcanic activity and erosion. These features may be a result of the way material which does not leave the hole cools and recondenses, leaving a surface which will influence how energy is absorbed on the next laser pulse.

(a)   (b)

Fig. 3.7. (a) SEM photomicrograph of hole drilled in stainless steel at 60° AOI and 1 J/cm^2 using a 350 μm spot, 5000 shots, and P polarization. (b) high-magnification view of the underside of the hole (the far end in (a)).

Another hole was drilled at higher fluence using a 280 μm spot at 3 J/cm^2 for 5000 shots (Fig. 3.8). The largest diameter of the circular holes in the bottom now reaches more than 30 μm. However, the grooves are not nearly as evident with a set barely visible along the right wall with about a 2 μm period. At still higher fluence, when a 200 μm spot and 6 J/cm^2 was used, the morphology of the hole changed dramatically, as seen in Fig. 3.9. The grooves and circular holes are still visible, but the hole bottom is mainly a deep central hole surrounded by very structured material (see also Section 3.9). Fig. 3.9(b) shows a higher-magnification picture of the walls of the central hole. The walls of this central hole are nearly perfectly circular and remarkably smooth. There appear to be concentric ridges as one goes deeper in this hole and additionally small (~30 μm) hemispherical nodules are present on the walls in an apparently random fashion.

Fig. 3.8. SEM photomicrograph of hole drilled in stainless steel at 60° AOI and 3 J/cm² using a 280 μm spot, 5000 shots, and P polarization.
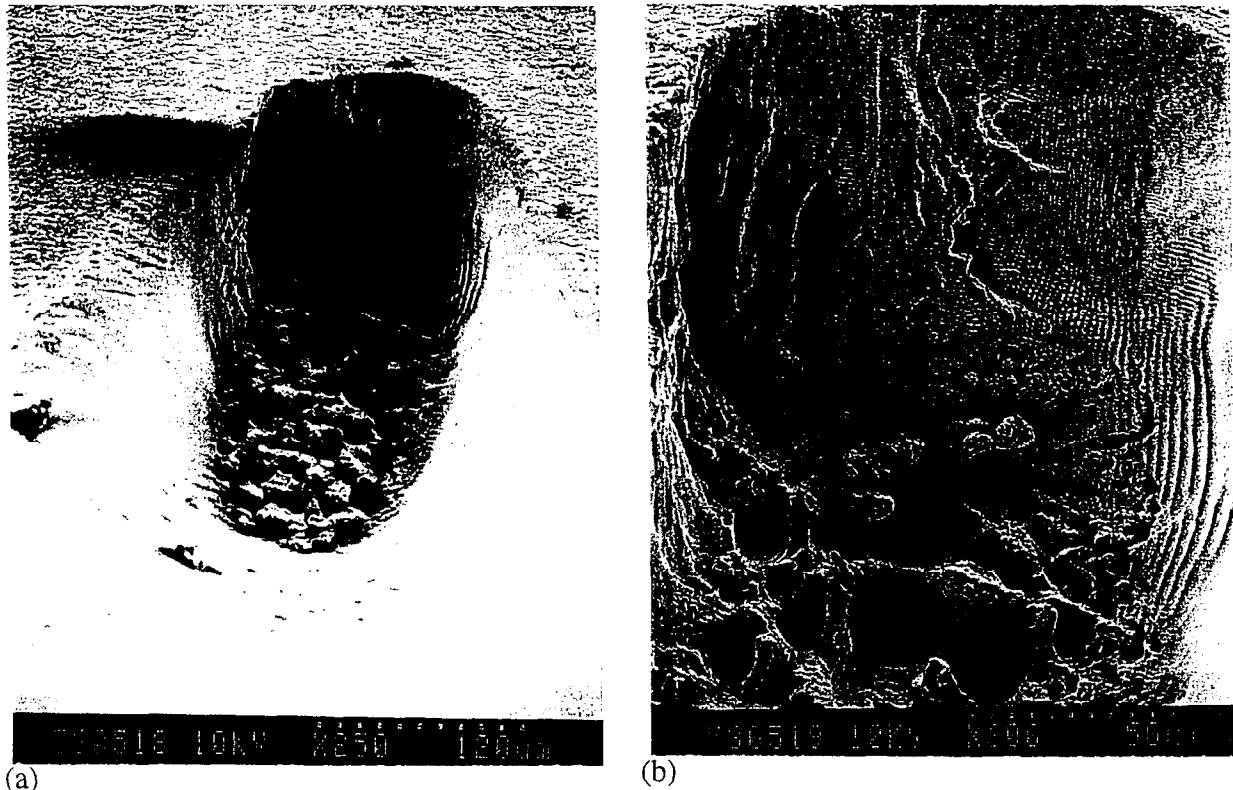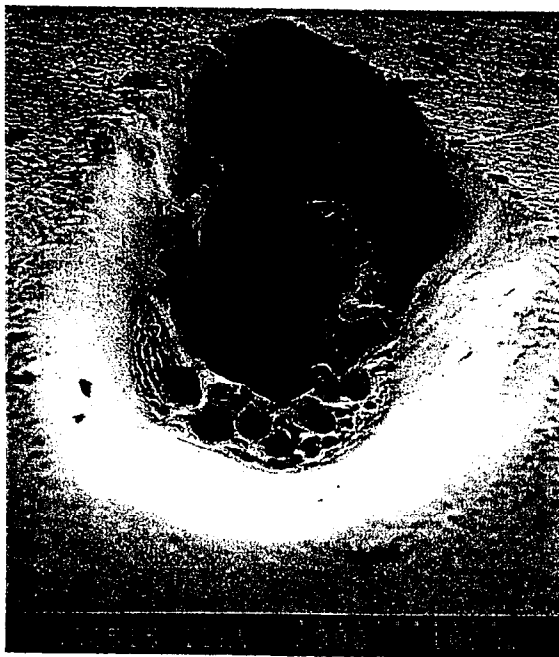

(a)

(b)

Fig. 3.9. (a) SEM photomicrograph of hole drilled in stainless steel at 60° AOI and 6 J/cm² using a 200 μm spot, 5000 shots, and P polarization. (b) close-up of a deep central hole in the middle of (a).

3.5 Polarization effects

We examined the effect of polarization on the drilling process for holes at $0°$ AOI and 1 J/cm^2. The drilling rates over the first few hundred microns were consistent with the rates obtained from holes drilled at $60°$ AOI, but the surface morphology of the hole bottoms differed. The hole drilled with linear polarization formed a much rougher surface near the center of the hole by 0.5 s (500 shots). Although polarization has a small effect on the holes near the surface, as the holes become deeper the hole shape is significantly affected by polarization. Fig. 3.10 shows optical photomicrographs of the exit faces of holes drilled in 300 µm thick, 316 stainless steel at $45°$ AOI for three polarizations: linear P, linear S, and circular. The beam diameter was approximately 110 µm, giving a fluence of roughly 5 J/cm^2. For linearly polarized light, the exit hole was elongated in the direction perpendicular to the laser polarization direction, but for circular polarization, the hole maintained its ellipticity. This is due to the difference in reflectivity for the S and P polarized light at high angles of incidence; light with a polarization component normal to the wall surface is absorbed more, resulting in less energy reaching the hole bottom on these sides. This means that there is less energy for ablation near the hole exit on the sides of the hole which are in the plane of polarization, and the exit in this dimension is smaller, resulting in an exit shape with a major axis perpendicular to the beam polarization vector. This effect becomes more pronounced as the sample becomes thicker. Other groups have reported unsatisfactory results with the use of circular polarization, preferring instead to spin a half-wave plate to randomize the polarization vector. We observed no significant difference between the two methods.

(a)   (b)   (c)
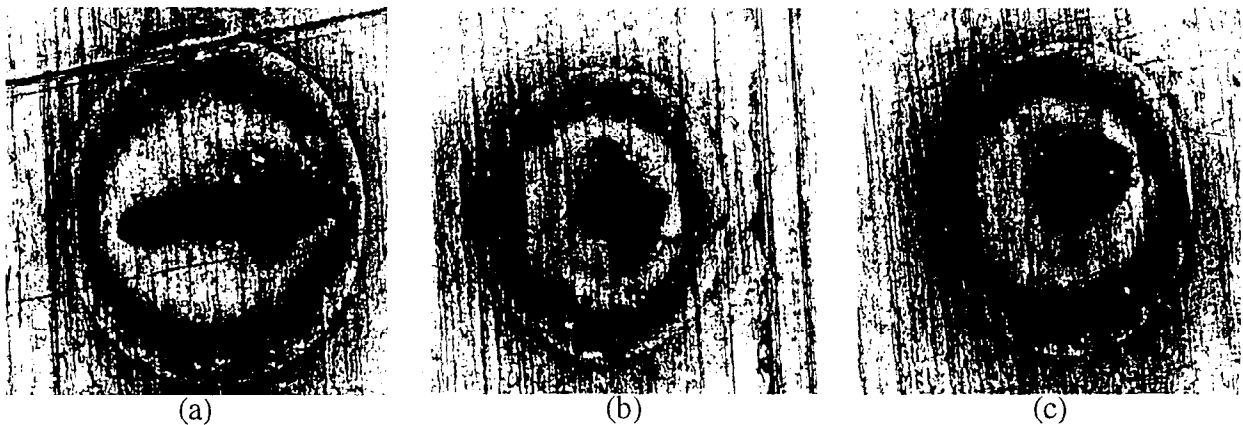
Fig. 3.10. Optical photomicrographs of the exit surface of holes drilled in 300 µm thick stainless steel at 5 J/cm^2 and $45°$ AOI using (a) vertical S-polarization, (b) horizontal P-polarization, and (c) circular polarization .

3.6 Structure on walls of slots

A 750-μm thick piece of tantalum was laser cut in two so that it was possible to look at the walls of the cut without further processing. The laser conditions were 15 J/cm^2, a 360 μm x 50 μm spot, 45° AOI, 150 fs, and circular polarization. Optical photomicrographs of the wall of this slot are shown in Fig. 3.11. In these pictures, the laser beam is incident from the upper left corner, and there are fine striations parallel to the laser beam propagation until approximately 120 μm from the initial plate surface on the left and about 340 μm from the initial surface at the top of the picture. At this point, these striations give way to grooves that run parallel to the original surfaces with a monotonically increasing period (from approximately 5 μm to 20 μm) with distance from the plate surfaces. These "rings", in turn, give way to more chaotic and pronounced grooves, again parallel to the beam direction, which extend to the exit face of the part. We observed the same type of structures in cutting SiC.

(a)   (b)

Fig. 3.11. Optical micrographs of side wall of slot cut in a 750 μm thick of tantalum showing formation of several groove-like structures. The magnification in (b) is 2.5X that in (a). The laser was incident from the upper left at 45°.

3.7 Formation of columns in ring cut

A small spot (approximately 100 μm in diameter) was trepanned using a spinning wedge in a circle about 3 mm in diameter. The laser light broke through the material (stainless steel) in small circular holes (see Fig. 3.12(a)) of 20–40 μm in diameter. Figure 3.12(b) shows a silicone casting made of this pattern showing the wall to be smooth for about one-half the depth, but then the highly regular circular holes are formed. The cause of this is unknown, but this behavior is similar to what has been observed in making line cuts using a circular or a line focus while scanning the part at feed rates of 0.5–5 μm/pulse. The light breaks through first in quasi-periodic holes which then coalesce with time. It may also be related to the behavior described in Fig. 3.9.
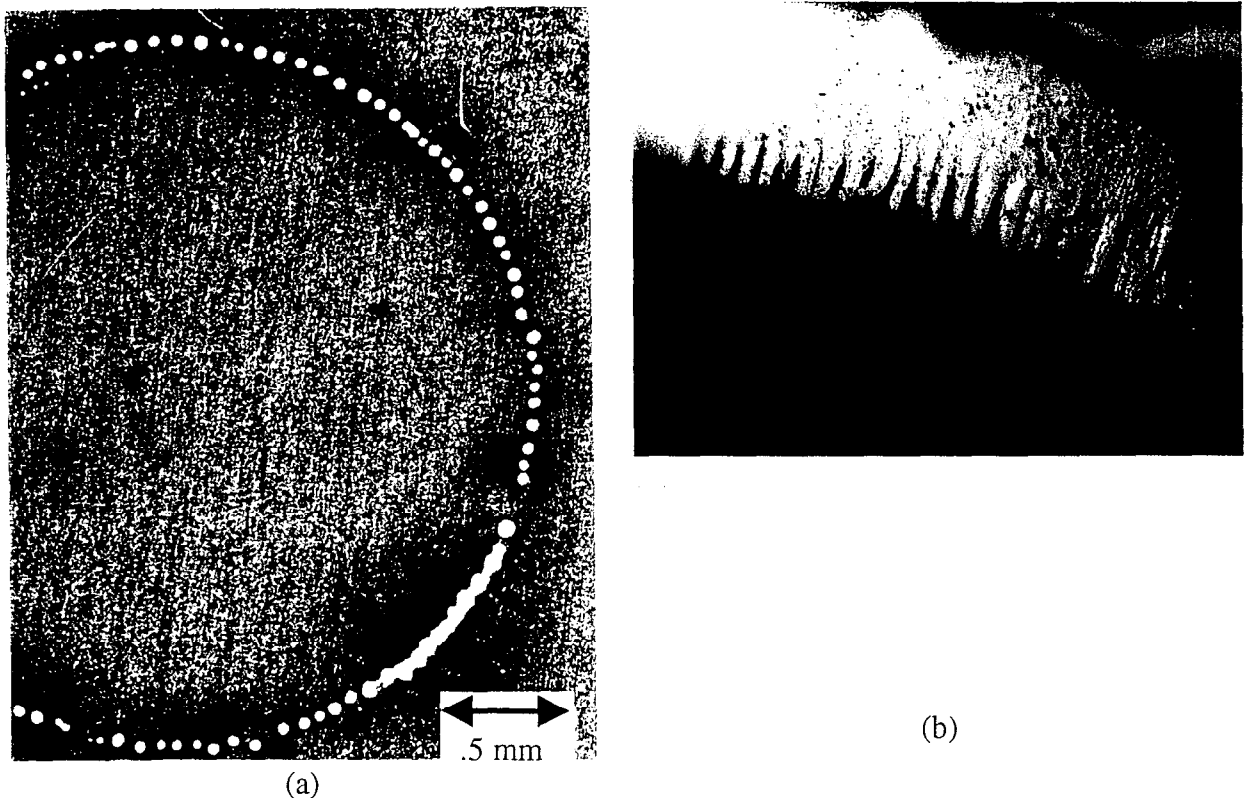

.5 mm

(a)

(b)

Fig. 3.12. (a) Optical micrograph of exit surface, and (b) silicone mold of ring cut.

3.8 Electric field effects

We looked at the effect of an electric field on the morphology of slots cut in stainless steel using a 370 μm x 50 μm line focus (15 J/cm^2) at 45° AOI with the major axis of the

30

line focus in the plane of incidence. The part was scanned back and forth to form a 1-cm slot and all slots were cut for 7 min. We used two configurations: 1) the part was grounded and a biased paddle was placed 2.5 cm in front of the workpiece, and 2) the part was isolated from the chamber and biased to a given voltage without the paddle present. Figures 3.13-3.17 show the resulting entrance and exit faces of slots cut in this manner with bias voltages of ±1000 V and ±2000 V. The applied electric field was deleterious when the workpiece formed the cathode of the circuit. The entrance surface took on a molten appearance and the exit slot became a series of holes rather than a clean slot (Fig. 3.13). When the workpiece was biased (negative), the effect was most severe. The exit surface displayed a series of craters indicative of some violent process occurring at the exit of the slot (Fig. 3.14). The effect of the applied field appeared to be negligible when the workpiece formed the anode (Figs. 3.15, 3.16). There may be a slight reduction in the raggedness of the edge of the exit slot when the part is grounded and the paddle is biased negatively (Fig. 3.15). Fig. 3.17 shows the effect of this bias after just one pass at 5 mm/s feed rate. Biasing the part positively caused essentially no change in the morphology of the slot while biasing the part negatively caused a drastic change to the cut quality. This behavior indicates that material removal is adversely affected by a field which acts to pull the electrons off of the workpiece.

A side note is that the morphology of the structure in the slot was independent of feed rate; it depended only on total exposure time. For example, 10 passes at 5 mm/s produced a slot with nearly identical morphology to 1 pass at 0.5 mm/s. The cause of the scale-like features in the slots is not known at present, but it may be due to stresses induced when the thin melt layer refreezes.
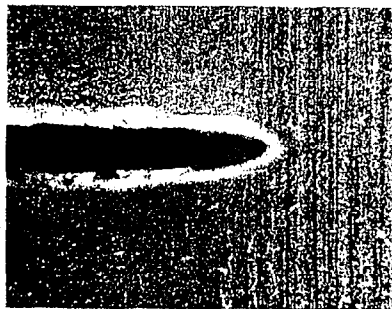
(a)   (b)   (c)
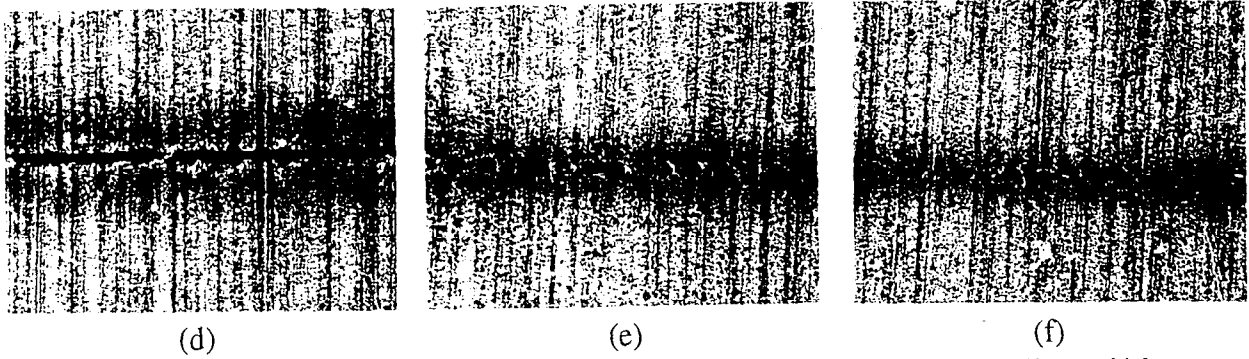
Fig. 3.13. Optical micrographs of entrance ((a)–(c)) and exit ((d)–(f)) surface of slots cut in 750 μm thick stainless steel at ground for no applied electric field ((a) and (d)), +1000 V 2.5 cm away from front surface ((b) and (e)), and +2000 V applied 2.5 cm in front of part ((c) and (f)).

Fig. 3.14. Optical micrographs of entrance ((a) and (b)) and exit ((c) and (d)) surface of slots cut in 750 μm thick stainless steel biased at -1000 V((a) and (c)) and -2000 V ((b) and (d)).

(a)

(b)

(c)
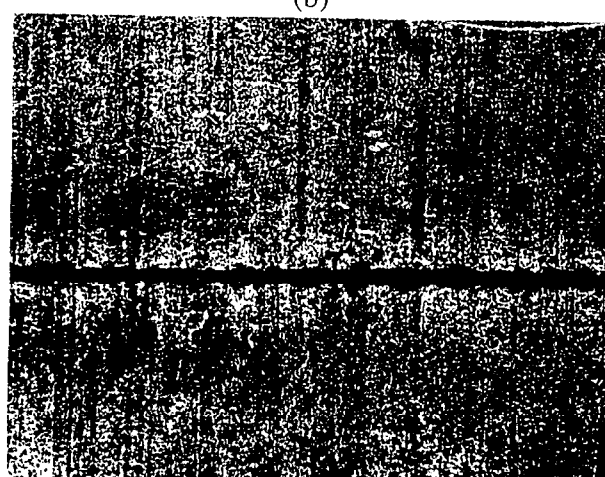
(d)

Fig. 3.15. Optical micrographs of entrance ((a) and (b)) and exit ((c) and (d)) surface of slots cut in 750 μm thick stainless steel at ground with applied field of -1000 V 2.5 cm away from front surface ((a) and (c)) and -2000 V applied 2.5 cm in front of part ((b) and (d)).

(a)

(b)

(c)

(d)
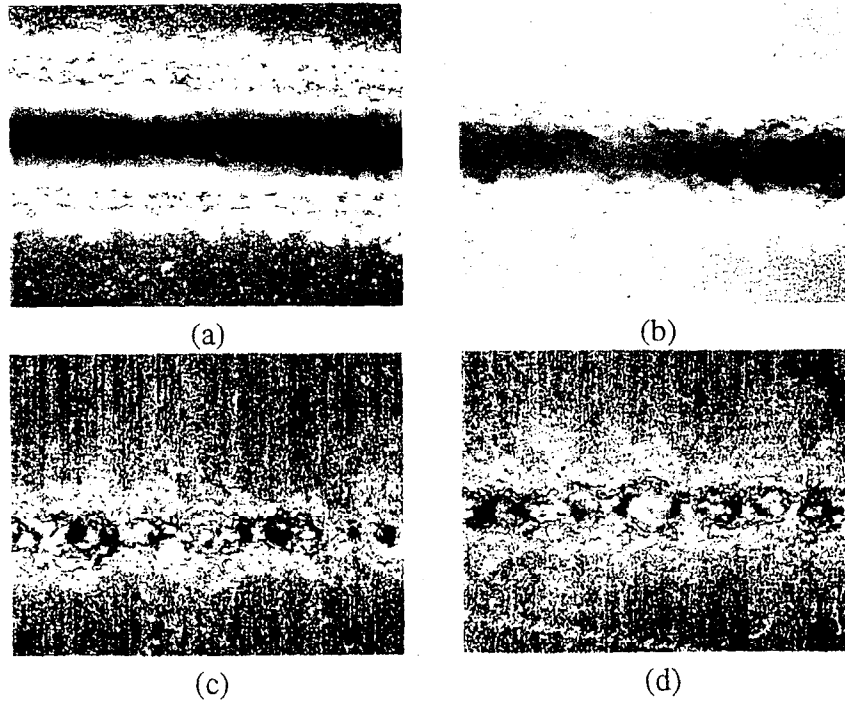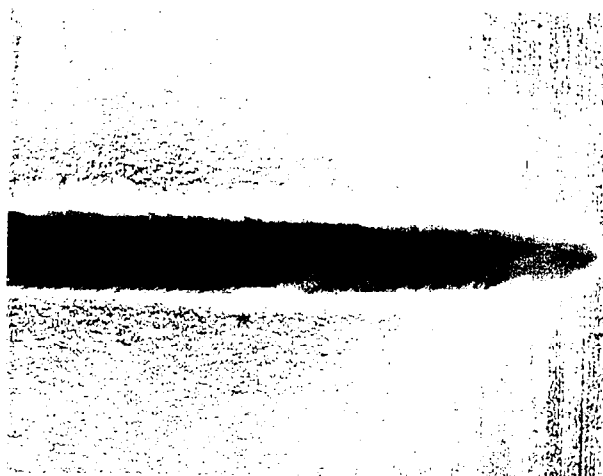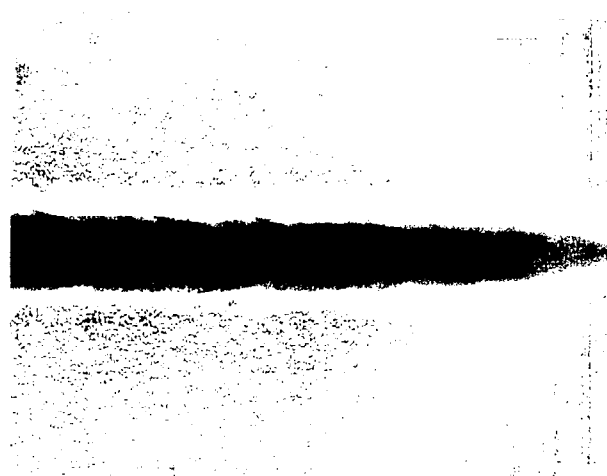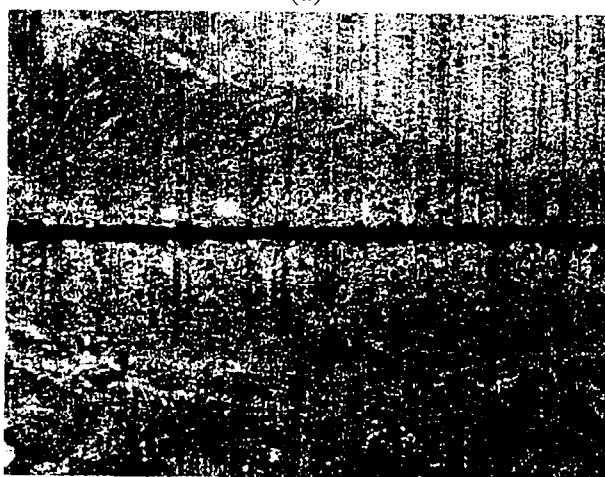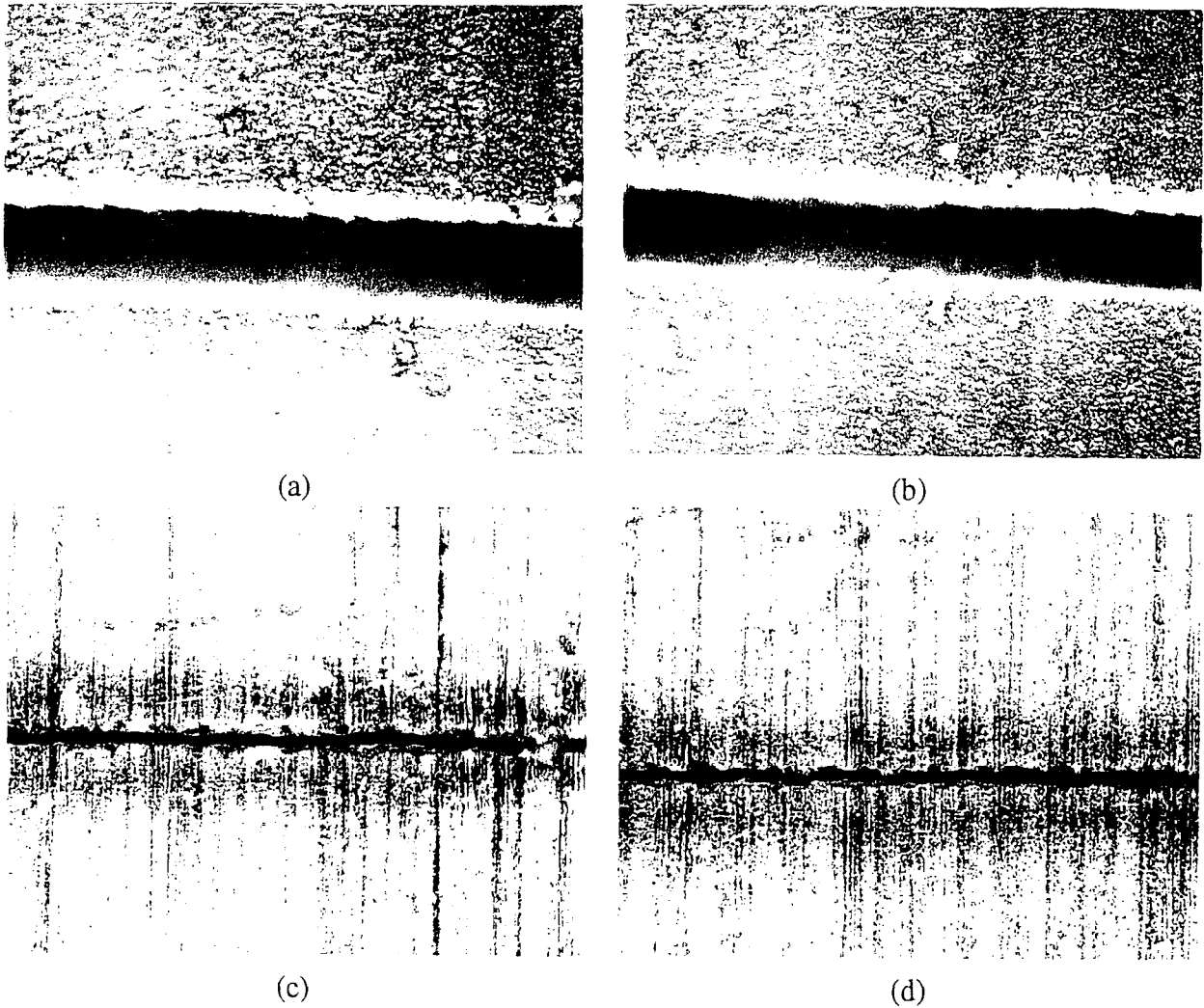
Fig. 3.16. Optical micrographs of entrance ((a) and (b)) and exit ((c) and (d)) surface of slots cut in 750 μm thick stainless steel biased at +1000 V((a) and (c)) and +2000 V ((b) and (d))

(a)

(b)

(c)
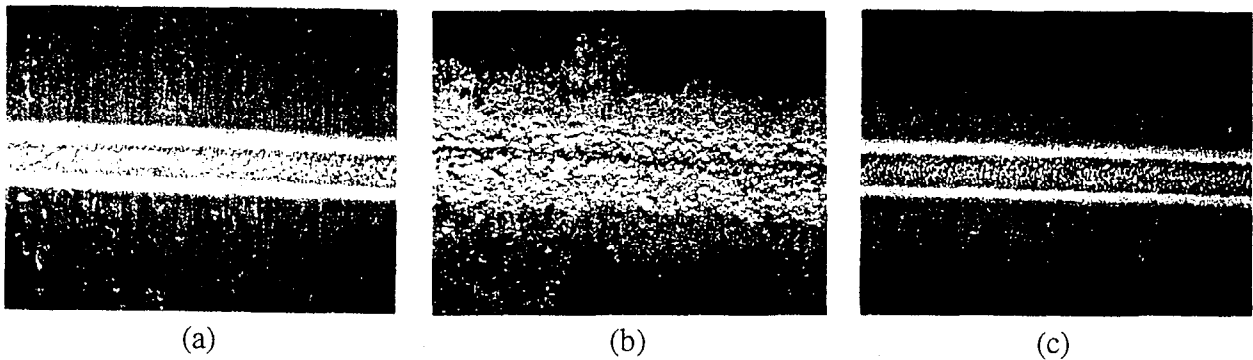
Fig. 3.17. Optical photomicrograph of surface of slot cut in stainless steel at 45° AOI after 1 pass at a feed rate of 5 mm/s for part biased at (a) +1000 V, (b) -1000 V, and (c) no bias.

3.9 Hole shape at high fluence

Several holes were drilled in 900-μm thick stainless steel (part no 093098-1). The holes were drilled for 5, 10, 15, 25, and 30 seconds (2 holes for each exposure time) at normal incidence and 10 J/cm^2 (2 W, 1 kHz, 150 fs). The polarization was circular (using a zero-order quarter waveplate) and the focusing lens' focal length was 33 cm. The transmission of the laser entrance window by the end of the set of holes was about 80%. The laser spatial profile was Gaussian with a diameter of about 230 μm (at 1/e^2 points).
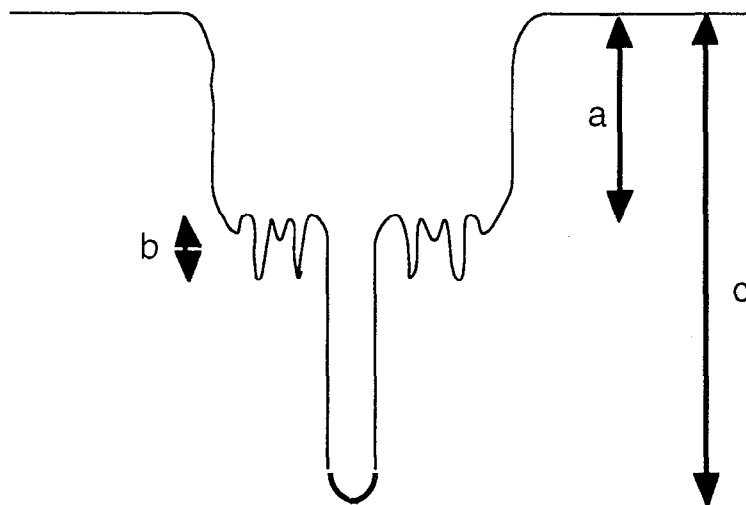
Fig. 3.18 Schematic representation of hole profile.

The part was removed and examined under the microscope. Each hole was approximately 400-430 μm in diameter at the entrance surface with the increase in diameter from the 5 s holes to the 30 s holes being about 20–30 μm. The holes exhibited an interior morphology represented in cross section in Fig. 3.18. SEM photomicrographs of two of the holes (5 s and 10 s) are shown in Fig. 3.19. There is a large diameter hole which extends a depth "a" into the part, ending in a rough-textured bottom. Then there is a small diameter hole located near the center of the hole which extends much deeper (a distance "c") into the part. This morphology was observed for all holes up to 20 s exposure time (20,000 pulses). For all of these cases, the diameter of the small, deep hole was 70-80 μm measured at its entrance.

Fig. 3.19. SEM pictures of holes drilled for 5 sec (top row) and 10 sec (bottom row). The right column contains enlarged views of the center hole.

36
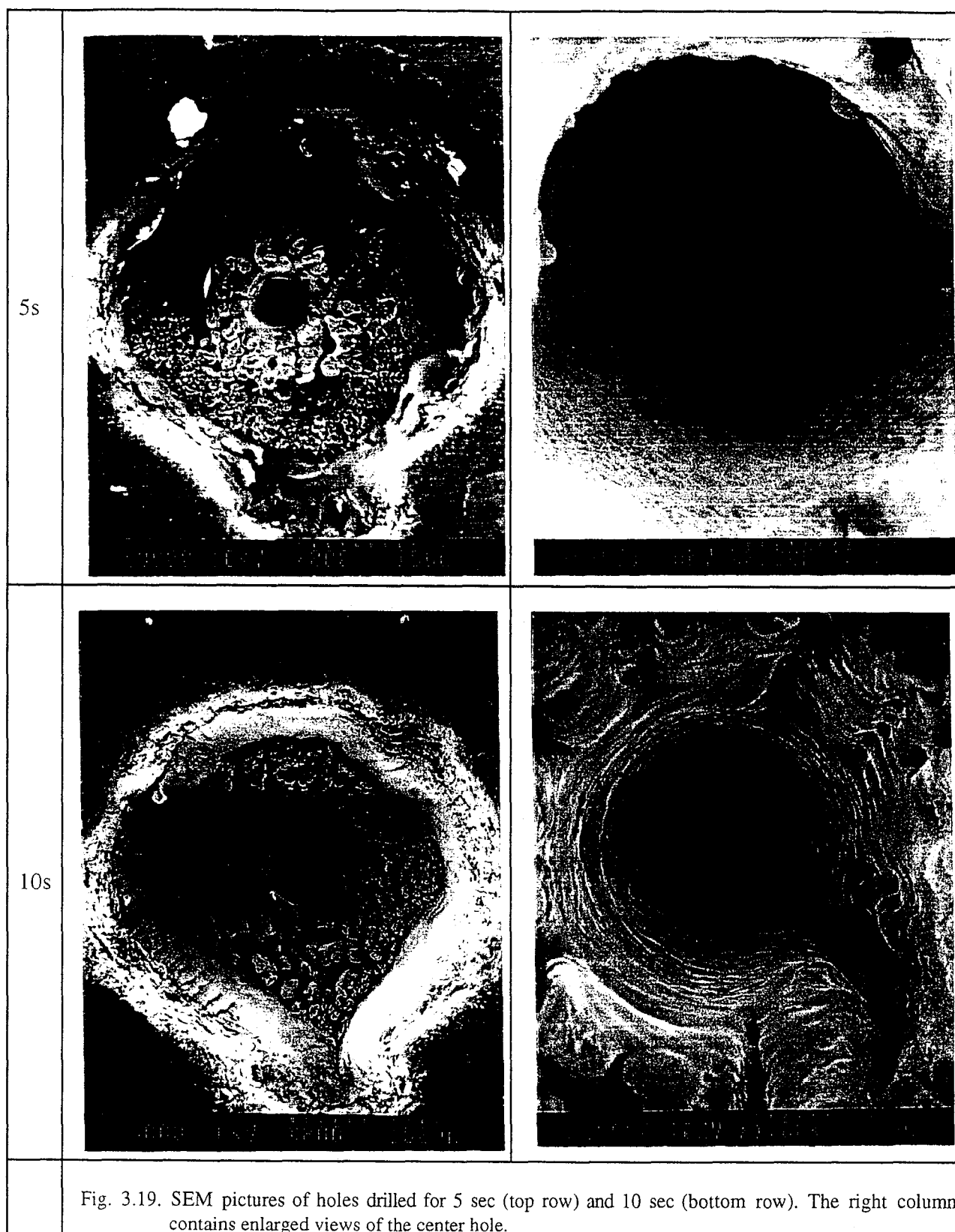
The vertical encoder on the optical microscope was used to measure the depths of each of these features at the different exposure times. The depths measured were consistent between the two holes drilled at each exposure setting. The results are as follows ("b" refers to the distance from the highest point of this rough bottom to the lowest point):

Exposure time (s)	a (μm)	b (μm)	c (μm)
5	120	50	350
10	290	70	570
15	450	60	900 (thru part)
20	610	120	900 (thru part)
25	900	n/a	n/a
30	900	n/a	n/a
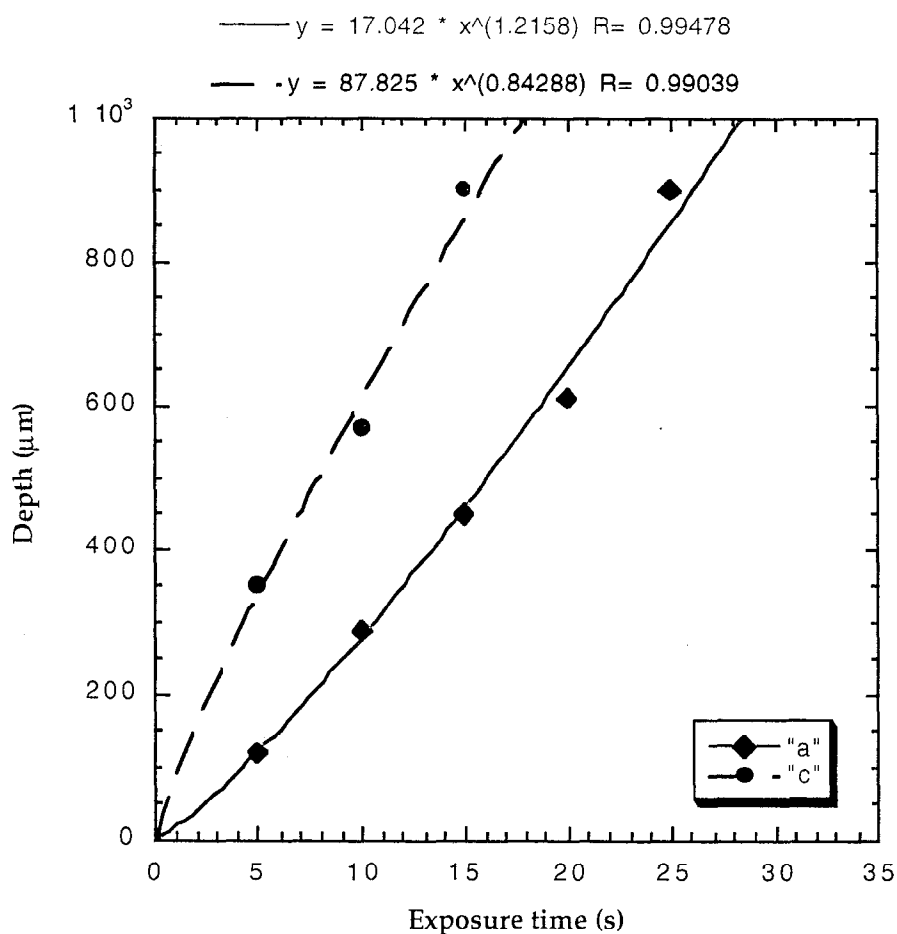
Fig. 3.20. Depth of hole features as a function of exposure time.

37

The depths "a" and "c" are plotted against laser exposure time in Fig. 3.20. By 25 seconds, the hole had been completely punched through, leaving only smooth side walls. Qualitatively, it has been observed that increasing the fluence by increasing the pulse energy decreases the time for first breakthrough but does not seem to significantly affect the time required to create a "clean" hole. This would indicate that higher fluence increases the growth rate of the filament ("c") but has much less effect on the growth rate of the main hole ("a").

It is not known what effects are involved, but the mechanisms must be fairly deterministic since the features and scale sizes were consistent over many holes. Further examination involving different pulse lengths, fluence, hole sizes, and polarization would be useful. This should provide information as to whether this phenomenon is intensity or fluence driven. Changing the spatial profile to more of a flat-top profile would also be interesting.

3.10 Transmission through drilled holes

Measuring the transmitted light during and after drilling a hole gives valuable information on the fraction of energy reaching the bottom of the hole. Holes were drilled at 45° through various thicknesses of 316 and 304 stainless steel. A power meter was placed in the imaging path so that the light passing through the drilled hole was collected by a ~30 cm lens (2 in. diameter). The meter was located to ensure that the collected light was entirely on the detector surface. The temporal behavior of the transmitted power was recorded as laser spot size, incident fluence, prepulse level, and material thickness were varied.

The transmitted power was usually not detected by the power meter until some time after breakthrough of laser light is visually observed. The power than gradually increased until a steady-state maximum was achieved. The transmitted power no longer increased even if the beam was left on the hole for several minutes after this point. At approximately the same time when steady-state transmission was reached, the plasma exiting the disappeared, suggesting that all ablation had stopped.

Figures 3.21-3.24 show the dependence of the steady-state transmission on the aforementioned parameters. In Fig. 3.21, the transmission is plotted as a function of fluence, parametric in material thickness (300 μm, 600 μm, and 1200μm), for holes drilled

38

with a 110 µm spot. The clusters of points represent all data points taken for a given fluence and thickness, including several prepulse levels (0% to 12%) with a 120 ps separation. As shown in Fig. 3.22, there is no obvious correlation between prepulse level and maximum hole transmission, but there is some scatter in the data. Transmitted light through the hole can be as little as 10% of the incident light for the 1200 µm thick samples. This means that a large amount of light is being absorbed in the walls (but no ablation is occurring), and that the amount of light reaching the bottom of a deep hole during drilling is only a small fraction of the incident fluence. This is very important when trying to drill particular hole shapes through thick material. It appears that there is a near logarithmic dependence on incident laser fluence of the transmission value for all thicknesses. It is not yet clear why this would be the case, but apparently the way the hole forms and the resulting transmission has some consistent functional dependence on the initial fluence.

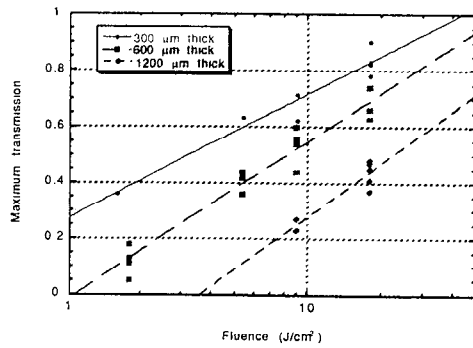Fig. 3.21. Steady-state transmission vs. fluence and thickness in 110 µm spot at 45° AOI.
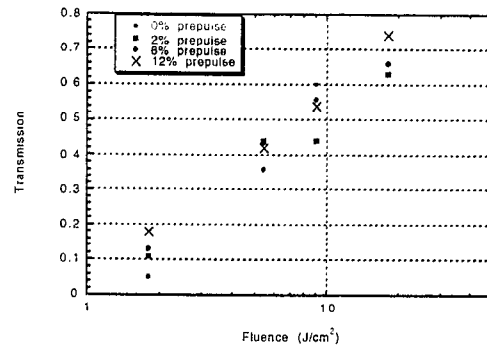

Fig. 3.22. Steady-state transmission vs. fluence and prepulse level for 110 µm spot in 600 µm SS at 45° AOI.
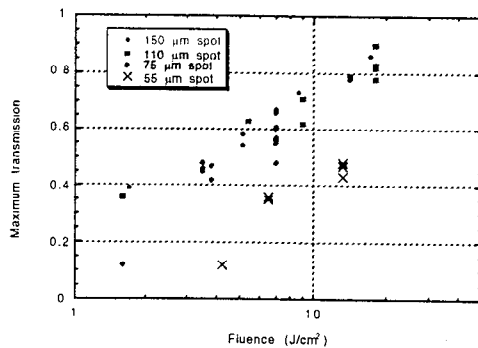

Fig. 3.23. Steady-state transmission vs. fluence and spot size in 300 µm SS at 45° AOI.
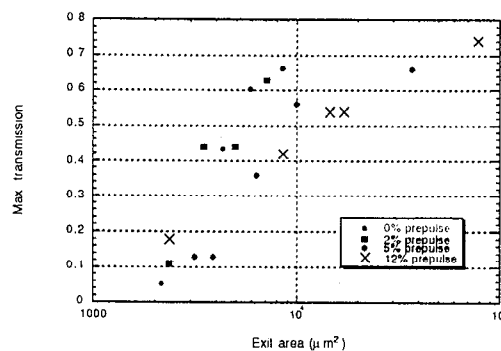

Fig. 3.24. Steady-state transmission vs. exit area and relative prepulse level in 600 µm SS and 110 µm spot at 45° AOI.

39

We also see in Fig. 3.21 that the transmission appears to exhibit an inverse exponential dependence on the material thickness. For example, at 20 J/cm^2 the transmission is 0.83 for 300 μm thickness, 0.68 for 600 μm thickness, and 0.44 for 1200 μm thickness. Each value is nearly exactly the square of the previous, i.e. as the thickness doubles, the transmission is squared. This similar to Beer's Law for transmission through an absorbing medium. Here however, the absorption must occur in the walls, and the diameter of the hole is not constant along the length of the hole so the relationship should be fairly complex. We have not yet developed any model which would explain this.

It might be thought that the smaller holes generated by smaller spot sizes might correlate with decreased transmission. However, as shown in Fig. 3.23 for 300 μm thick material, there is little dependence on spot size until the 55 μm spot size is reached (except for the one point for the 75 μm spot at 2 J/cm^2). Conversely, as seen in Fig. 3.24, the final transmission is highly correlated with the exit area of the hole (and also the entrance area) as measured at the exit face. There must some interplay between the spot size and the natural hole size for a given fluence that makes the absolute dependence on spot size minimal. It can also be seen in Fig. 3.24 that the holes generated with a beam with a 12% prepulse transmit significantly less for the same exit area. Again, the cause of this has not been investigated further.

The following are some general observations with regards to these transmission experiments:

1) The polarization of the light emerging from the holes was checked by inserting a polarizer between the hole and the power meter, using a waveplate to measure both S and P polarization emerging from the hole. The ratio of S/P was unchanged when the part was removed indicating that propagation through the hole does not effect polarization (incident polarization was elliptically polarized).

2) Holes were drilled using S polarization at 45° AOI with a line focus (70 μm x 700 μm) in 600 μm SS with laser left on until well after all ablation had stopped. Power was reduced, and the transmitted power was measured for S, P, and circular incident polarization. No change in relative transmission was observed for the different polarizations.

3) However, if a similar hole is drilled using P polarization until ablation has essentially stopped, and then the polarization is rotated to S (rotating waveplate), ablation begins

again and the transmission increases (more than 2X). As mentioned above, if power is reduced significantly before changing to S, there is no effect on the relative transmission.

4) A hole was drilled and maximum transmission was recorded. The incident power was reduced, but no change in relative transmission was measured.

5) For a set of 3 holes drilled in 600 μm SS using a line focus (70μm x 700 μm, 8 J/cm^2, 45°AOI, 12% prepulse 500 ps in front of main pulse) and S, P, and circular polarization (one hole with each polarization), the transmission of the hole drilled with P is less than half that of those drilled with S or circular (0.14 vs. 0.33 for C and 0.28 for circular). The breakthrough times for these holes were 85 s, 125 s, and 85 s for S, P, and C, respectively. However the entrance holes are essentially the same size, and the exit hole width for the hole drilled with P is twice that of the other two holes. See Fig. 3.25.

6) When a hole is drilled until ablation stops (no plasma light visible), the shutter in front of the chamber is closed momentarily and then reopened, ablation (plasma is observed) is observed for a second or two.

7) Typically, as a hole is drilled in SS, the plasma begins as a bright blue color, gradually changing to a powder blue and then to a dirty white/brown. For the holes drilled with a prepulse, the plasma retains the bright blue color for a longer time.

Exit   Entrance (1/2 magnification)
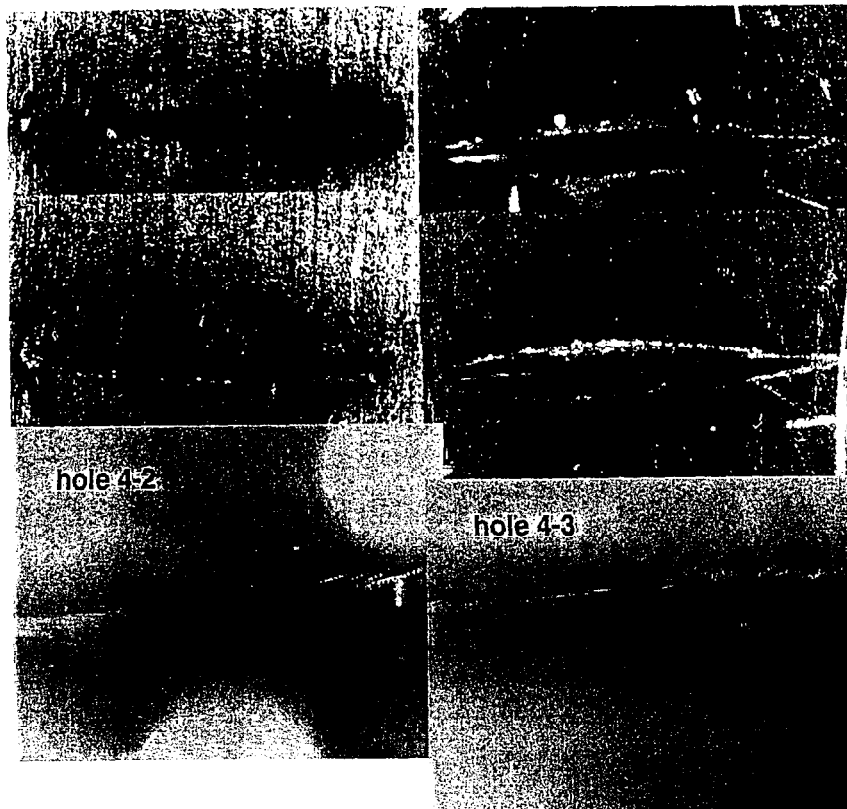
Hole drilled with S pol.
Exit is 40μm X 820 μm.

Hole drilled with P pol.
80μm x 800 μm.

These two are the interior
of the holes (S pol on the
left) at 2X magnification
of the exit surface.

Fig. 3.25. Photomicrographs of holes mentioned in point 5.

3.11 Drilling of small holes

We performed a preliminary investigation into the possibility of using short-pulse (100 fs) lasers for micro-drilling of ICF capsules. In this approach to filling NIF targets, an extremely small hole would be drilled in the ablator shell, the target would be filled with DT fuel, and the hole sealed. To minimize perturbations upon compression, it is desirable to drill the hole as small as possible and with minimal slag or heat-affected zone. The goal is to drill sub-5 μm diameter (preferably <2 μm) holes through 100-150 μm thick Be. This is an ideal situation to employ femtosecond laser processing due to the negligible thermal loading on the part.

In initial experiments, holes were drilled in 125-μm thick Be foil using a 1-kHz, 120-fs, Ti:sapphire short-pulse laser system. Numerous combinations of spatial filtering, focus lens, f#, and wavelength were tried and the best focal spot obtained was 5 μm $1/e^2$ diameter. To achieve this, the laser output was spatially filtered, frequency doubled to 413 nm, spatially filtered again, and then focused with a 25-mm focal length GRIN lens (LightPath) at approximately f#=5. Both the quality of the BBO doubling crystal ($\lambda/2$ surface) and the choice of focusing lens leave room for reducing the focal spot size.

The Be foil was mounted on a xyz-translation stage in a vacuum chamber pumped down to 25 mTorr. A scan in focal position was performed and SEM images of the smallest hole obtained are shown in Figure 3.26. The entrance diameter is approximately 5.5 μm. A thin film of ejected material is evident around the hole and although no attempt at cleaning was made here, it is our experience that these films easily wipe off. The exit hole is 3 μm diameter giving a taper angle of only 0.6°. This hole was drilled with ≈1.8 μJ pulses (18 J/ cm^2) at 1 kHz in 12 seconds. Initial results on foils are very encouraging. We will work to improve the focal spot as holes <2 μm should be possible with a smaller f# and possibly third harmonic.

(a)
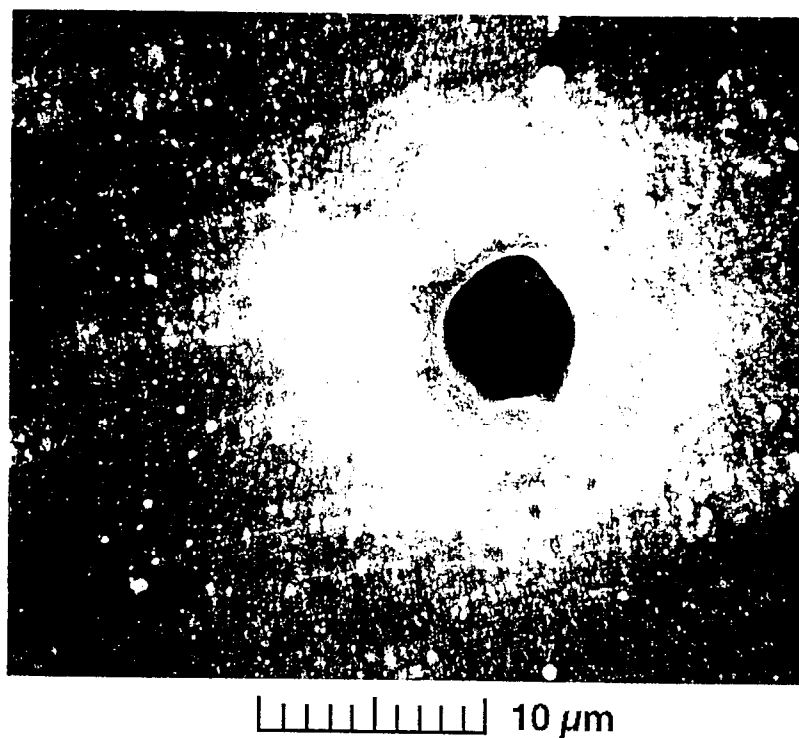
(b)
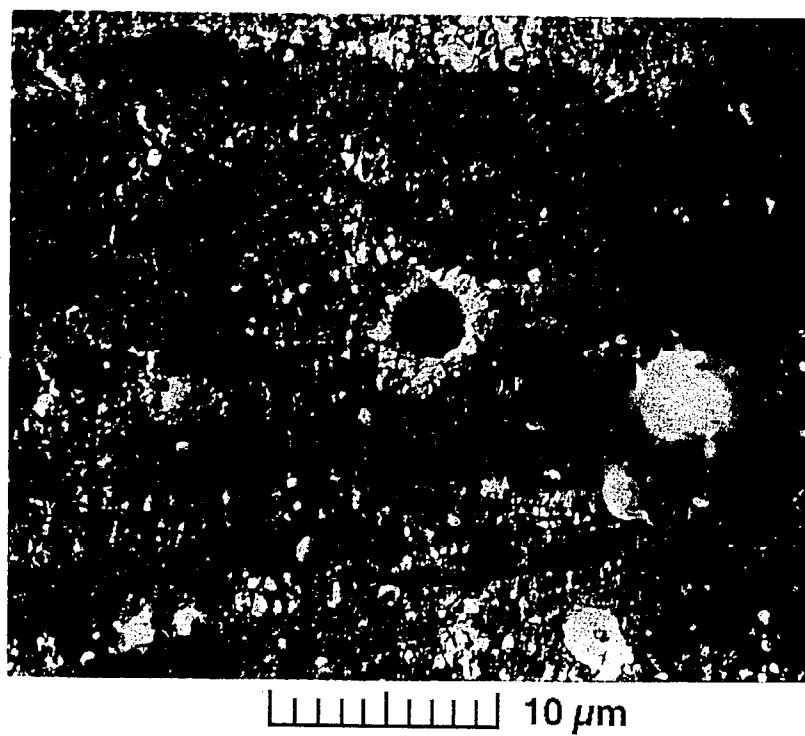
Figure 3.26. SEM images of (a) entrance, and (b) exit holes drilled through 125-μm thick Be foil.

3.12 Repetition rate effects on hole drilling

We drilled several holes in 1-mm thick metal at 150 fs using a quasi-flattop beam created using a phase plate. The initial 1 kHz repetition rate was reduced to 500 Hz and 200 Hz using a Pockels cell and polarizer. The energy level of the leakage pulses was one-hundredth that of the main pulses in the pulse train and could be neglected. Two beam sizes (approximately 250 μm and 550 μm at a fluence of 5 J/cm^2 and 1 J/cm^2, respectively) were used to drill the holes, and the spatial profile did change somewhat because of the phase plate. The drill rate was measured using the actual hole length along its axis and the time to first detection of breakthrough. The holes drilled at 1 kHz were done several times with the breakthrough times agreeing to within 1 s, but at the others repetition rates, only one hole was drilled. In Fig. 3.27, it can be seen that for the larger holes, the rate is essentially independent of repetition rate, but for the smaller holes, the rate actually increased with repetition rate. This may indicate some influence by long term thermal effects made more prominent with decreasing hole size.
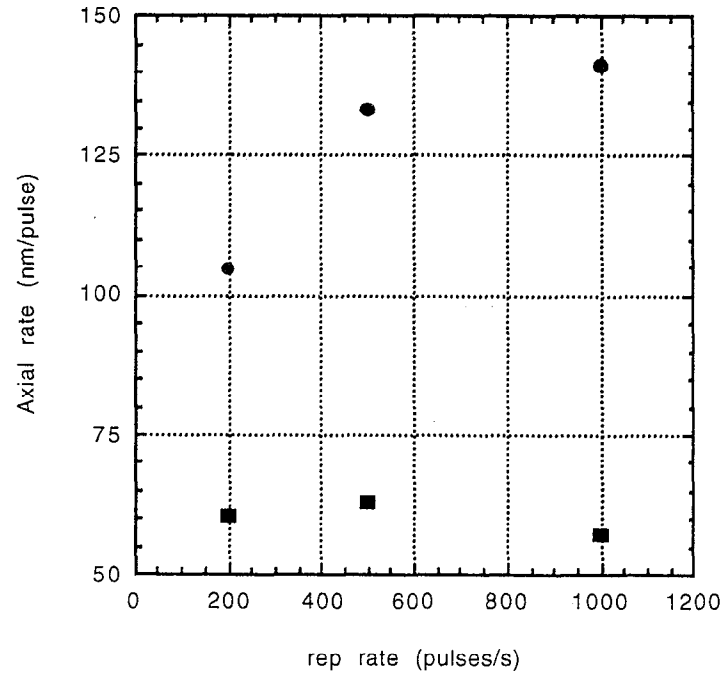
Fig. 3.27. Drilling rate as a function of pulse repetition rate. The red dots are for a 250 μm diameter spot and the blue squares are for a 550 μm spot.

45

4. Effect of prepulse on machining of metals

High average power, chirped-pulse amplification (CPA) systems required for short pulse materials processing typically use a regenerative amplifier. This component, in particular, can produce prepulses from leakage at each round trip as well as from spectral modulation. Depending on the mechanism, the separation between the prepulse and the main pulse can be from ~ 1 ps to 10–20 ns. The presence of this prepulse will form a plasma prior to the arrival of the main pulse, resulting in a laser-plasma interaction which could adversely affect the machining process. Because of this, we examined the effect that prepulses can have on both drilling rates and hole quality for drilling holes in stainless steel.

4.1 Experimental

These experiments were done using a Ti:sapphire laser system based on chirped-pulse amplification (CPA) which produces 150 fs pulses with energies of up to 6 mJ at 1 kHz. All detectable prepulses were eliminated from the system, and a controlled, collinear prepulse was introduced using an optical system shown in Fig. 4.1. The main pulse was split with a beam splitter (30% transmission), and the two pulses were then recombined
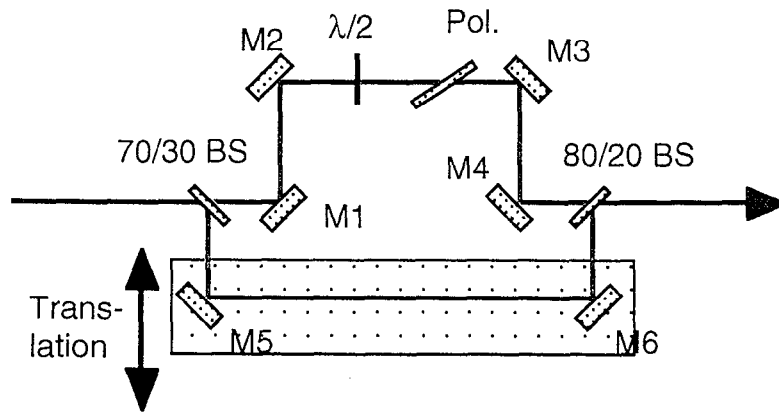
Fig. 4.1. Schematic of optical assembly used to generate prepulses. The components are two beamsplitters (BS), six mirrors (M), and a waveplate ($\lambda/2$) and polarizer (Pol).

with another beam splitter (20 % transmission). A waveplate/polarizer combination in the prepulse leg made it possible to continuously vary the relative energy in the prepulse from 0 to 12%. This ensured that the prepulse and main pulse were of the same polarization even though the throughput was reduced to approximately 60%. A rail was used to vary the path length traveled by the main pulse in order to vary the temporal separation between the two

46

pulses from 0 to 6 ns. We used this arrangement to study the impact of a prepulse on cutting rates and hole quality as a function of the main pulse to prepulse separation $\Delta\tau$, relative prepulse level, fluence, and hole size.

4.2 Prepulse results

We first used a line focus (70 μm $\times$ 700 μm with the long axis parallel to the plane of incidence) and measured the time required to drill through 600 μm of stainless steel at 45° and 8 J/cm^2 as a function of pulse separation and incident polarization. The prepulse energy was set to be 12% of the main pulse energy, and the temporal separation was varied from 0 to 6 ns; the spatial overlap of the two pulses was checked at each point. The resulting drilling rates, calculated as the material thickness measured along the axis of the hole (e.g.
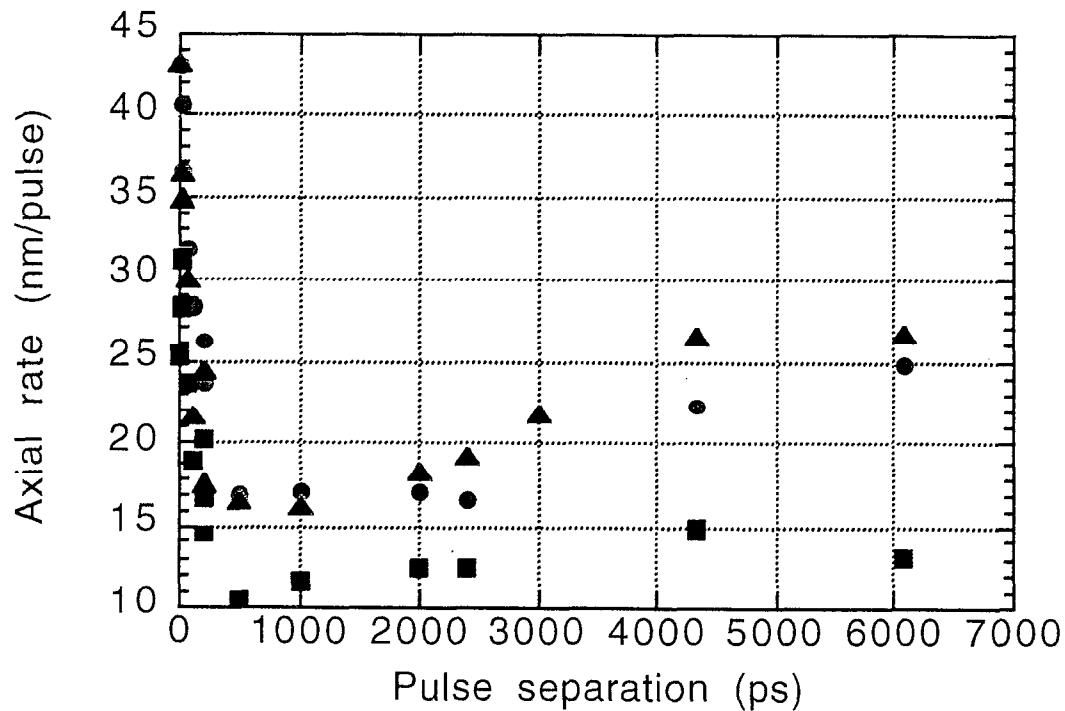
Fig. 4.2. Drilling rates (measured by breakthrough time) for holes drilled in 600 μm stainless steel at 45°, 8 J/cm^2, and 12% prepulse: circles—linearly polarized-S, squares—linearly polarized-P, and triangles—circularly polarized.

at 45° AOI, this is the sample thickness multiplied by 1.4) divided by the time when light is first observed through the hole at the exit face, are shown in Fig. 4.2 for three polarizations: linearly polarized S, linearly polarized P, and circularly polarized. For all cases, the presence of a prepulse significantly decreases the drilling rate, with the maximum effect occurring near 1 ns pulse separation. Drilling rates as measured by the time at which

the transmission through the hole reaches 70% of its maximum or steady state value show similar behavior, with the decrease for P-polarization being especially large. From regenerative amplifiers, leakage from the polarizer each round trip typically produces prepulses separated by 10–15 ns. From the trends in Fig. 4.2, it is apparent that for circular and S-polarized light, any effect from prepulses generated in this fashion is likely to be minimal, particularly in light of the fact that such prepulses are not likely to be 12% of the

(a)   (b)
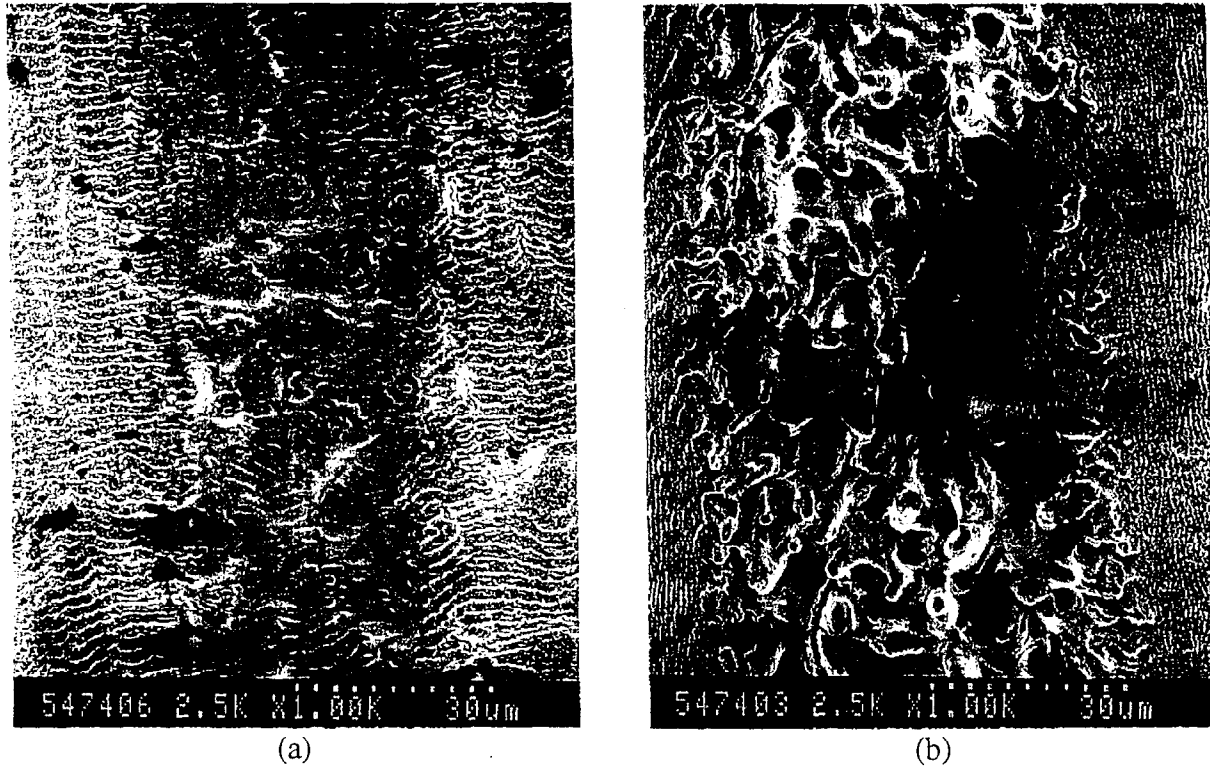
Fig. 4.3. SEM photomicrographs of surface of holes after 200 pulses drilled at 45° AOI and 8J/cm^2 for (a) P-, and (b) S- linear polarization.

main pulse (more likely <1%). However, the drilling rate for P-polarized light appears to remain low for a longer period of time and is more likely to be affected by prepulses separated by on the order of 10 ns.

Our theoretical calculations (Section 2.2.2) suggested that resonance absorption effects at pulse separations of approximately 10-20 ps would lead to increased absorption of the incident laser light, possibly leading to more efficient removal of material and an increased drilling rate. However, we observed no such beneficial effect—the decrease in rate from 0 to 1 ns is monotonic for all three polarizations. As discussed previously, our modeling

48

capability is limited to pulses incident on a planar surface and as such may not correctly describe the evolution of the hole past the first few pulses. Because of this, we also
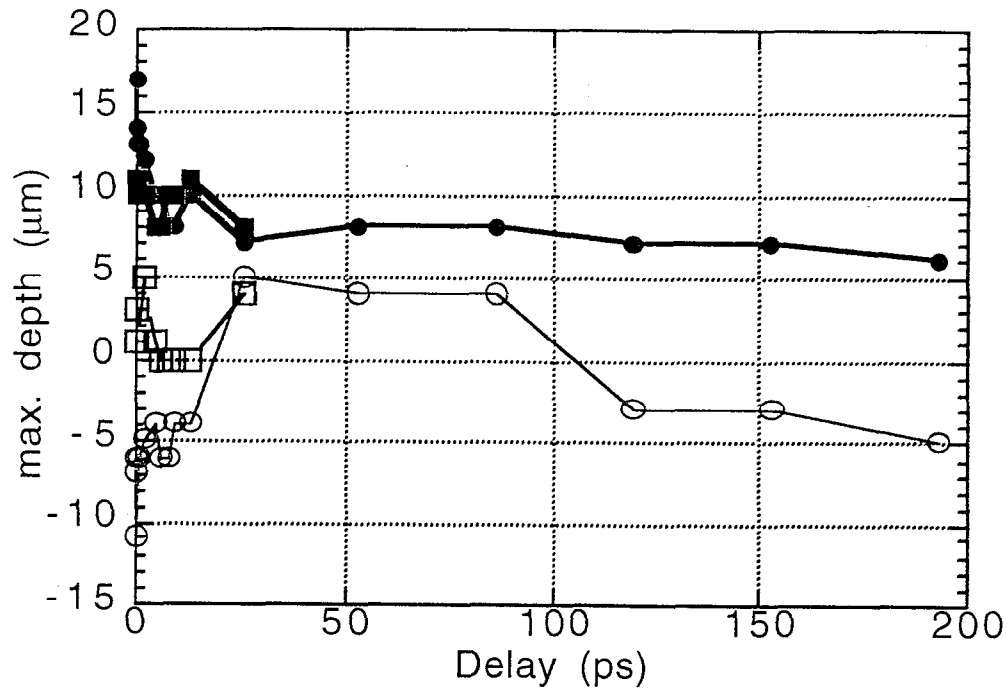
Fig. 4.4. Depths of lowest and highest features on hole bottoms after 125 pulses for S polarization (circles) and P polarization (squares). In this graph, positive is below the original surface and negative is above. The open symbols indicate the highest points.

examined the effect of prepulses on the hole evolution over the first few hundred pulses. The measurement of drilling rates is complicated by the fact that for many cases, the bottom surface of the hole quickly becomes rough, with the size of the roughness being somewhat correlated with fluence. Examples of some of the surface morphologies observed in this regime are seen in the SEM photomicrographs shown in Fig. 4.3. The same 70 µm x 700 µm beam as above was incident on a stainless steel coupon at 45° and 8 J/cm^2 for 200 pulses with P-polarized light making the hole shown in Fig. 4.3(a) and the hole from S polarization shown in Fig. 4.3(b). Circular polarization creates a hole with a bottom morphology similar to that of Fig. 4.3(a), although with less roughness.
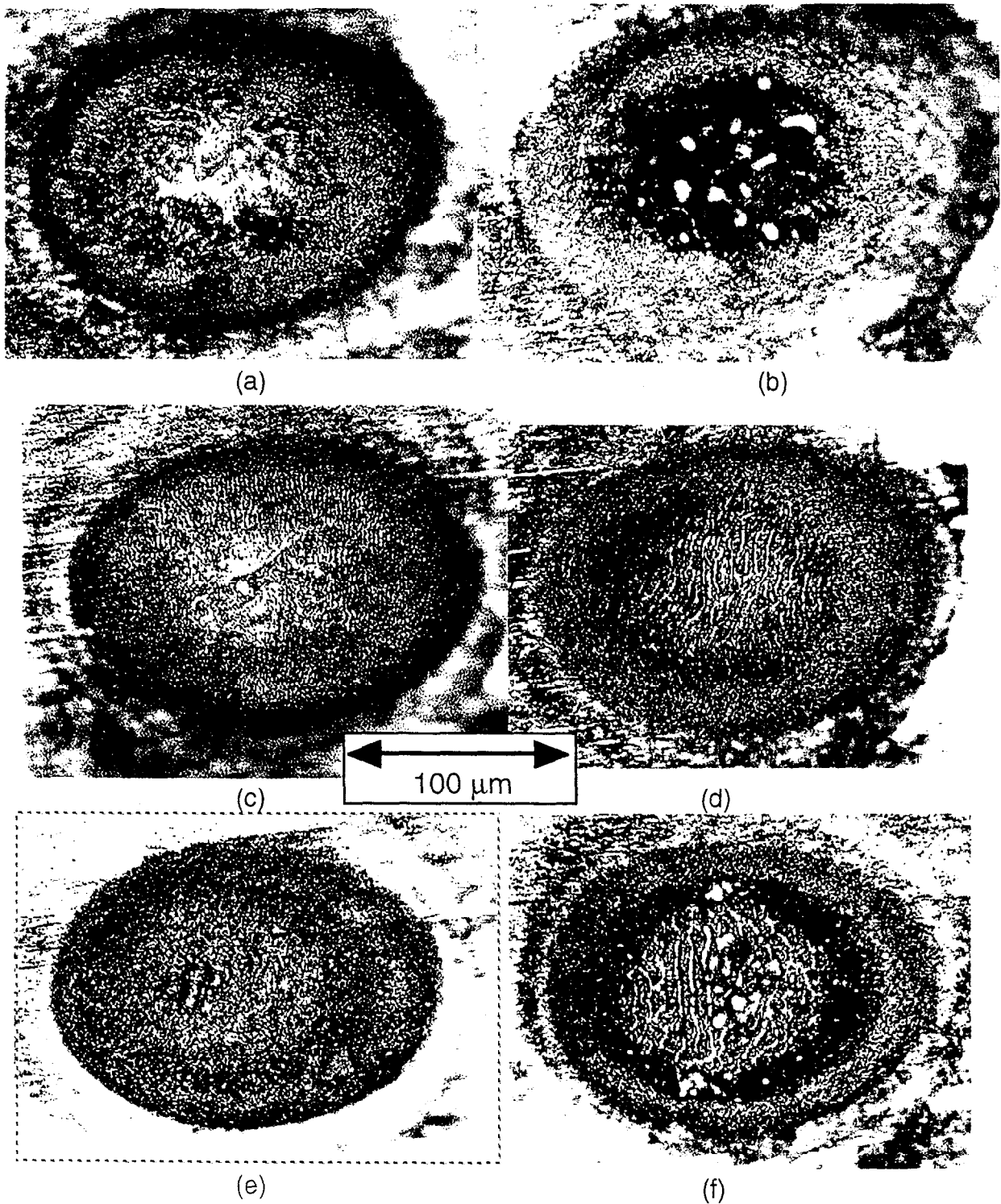
Fig. 4.5. Photomicrographs of bottom surfaces of holes after 125 pulses for no prepulse ((a) and (b)), a 25 ps prepulse ((c) and (d)), and a 200 ps prepulse ((e) and (f)). (a) and (c) are for P-polarized light; (b), (d), and (f) are for S-polarized light; and (e) is for circular polarization. As these pictures are displayed, the laser is incident from the left at 45° AOI.

Other holes were drilled at 45° AOI in stainless steel using a 100 μm round spot, and 7 J/cm^2, while varying the delay between the main pulse and the prepulse (12% of main pulse energy). The depth of these holes was measured using an optical microscope with an encoder on the vertical or focus axis and an objective with a depth of focus of less than 1μm. In many cases, the highest point of the structure at the bottom of the hole was above the original surface of the material. These measurements of vertical position of the highest and the lowest points located within the hole are plotted in Fig. 4.4 as a function of the separation $\Delta\tau$ between the main pulse and the prepulse. As before, the presence of a prepulse decreases the drilling for all observed values for $\Delta\tau$ with no apparent effect due to resonance absorption. However, a point of interest is that although the drilling rate is decreased (determined by the deepest point in the hole), a prepulse while using S-polarized light decreases the size of the structure in the hole bottom and produces a smooth bottom when $\Delta\tau = 30$–80 ps. We have not had the opportunity to investigate the cause of this further. Fig. 4.5 shows optical photomicrographs of the surface morphology for these 125-shot holes for S- and P-polarizations for no prepulse, $\Delta\tau = 25$ ps, and $\Delta\tau = 200$ ps (S-polarized only). The change for S-polarization is quite dramatic as the pulse separation is increased.

In addition to examining the effect of the pulse separation $\Delta\tau$, we also looked at the effect of a prepulse at a fixed value for $\Delta\tau$ (120 ps) while varying fluence, spot size, thickness, and relative prepulse energy. We used two different methods for calculating a drilling rate: the first using the time to first detection of breakthrough and the second using the time for the light transmitted through the hole to reach 70% of its maximum value. This latter value was measured using a power meter positioned to collect all of the light transmitted by the hole which exits the vacuum chamber. The transmitted power increases in some fashion after breakthrough until it reaches a maximum (see Fig. 4.6) at which
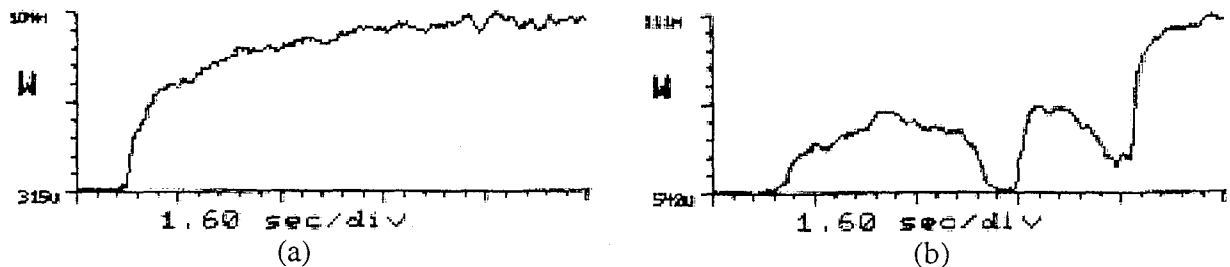

Fig. 4.6. Transmission through hole drilled in 300μm thick stainless steel with a 75 μm spot and 10 J/cm^2. (a) no prepulse, and (b) 12% prepulse 120 ps in front of main pulse. The maximum transmission without the part is 185 mW.

51

time it is no longer possible to visibly detect any plasma leaving the hole, i.e. ablation ceases. When a prepulse is present, even though breakthrough may occur early on, the transmitted power tends to remain at a low level until a very sudden increase to the steady-state value. In fact, the hole can close and reopen several times until this point is reached (see Fig. 4.6(b)). For no prepulse, on the other hand, the increase in transmission tends to be relatively gradual beginning almost immediately after breakthrough (Fig. 4.6(a)). The choice of 70% as the threshold was arbitrary and was mainly chosen to avoid the oscillating maxima seen in Fig. 4.6(b) prior to the actual end of ablation while avoiding the gentle slope at higher relative transmission seen in Fig. 4.6(a).

Figure 4.7 shows the drilling rate at 45° with a 110 µm spot and circular polarization as a function of fluence for three different relative energies levels of prepulse (0%, 6%, and 12%), and for three different thicknesses of material: (a) 300 µm, (b) 600 µm, and (c) 1200 µm. The rates determined by breakthrough times and by 0.7 T_{max} are shown in these figures by filled and open symbols, respectively. Each point for the breakthrough rate represents an average over 3-7 holes with the larger rates being subject to larger uncertainties since these rates correspond to drill times of 1–2 s and timing was done manually. The presence of a prepulse also greatly increased the scatter in the breakthrough times with ranges of 50% of the mean value common. For the rates determined by transmission threshold, the points represent only 1–2 samples since fewer transmission measurements were made. However, the transmission through all of the holes drilled was monitored on a CCD camera and the time at which this observed light reached steady-state was recorded manually. Although this method was much more subjective, for most conditions the rates determined by the two transmission methods agreed to within 10%, and the scatter was typically of the same order (10–20%). Finally, measurements, particularly with no prepulse, were repeated occasionally over the experimental period of several months, and we found that the repeatability of the measured rates was excellent.

These graphs in Fig. 4.7 show that for the thinner materials and low fluence, there is no significant effect on drilling rate by a prepulse. However, as the fluence is increased above 6 J/cm^2, the drilling rate increases more slowly with larger prepulses. In fact, for the rate defined by the 70% transmission criterion, the rate decreases with fluence. This would indicate that there is a threshold fluence for the prepulse to have an effect, and as the main pulse fluence increases so does the prepulse fluence and the effect becomes more pronounced. The effect also becomes more pronounced as the material becomes thicker.

52

Fig.4.7(a). Drilling rate through 300 μm thick 316 stainless steel. The prepulse levels are 0% (circles), 6% (squares), and 12% (triangles). Breakthrough rates are the closed symbols (and thicker lines) and transmission rates are the open symbols (and thinner lines). 45° circular polarization.
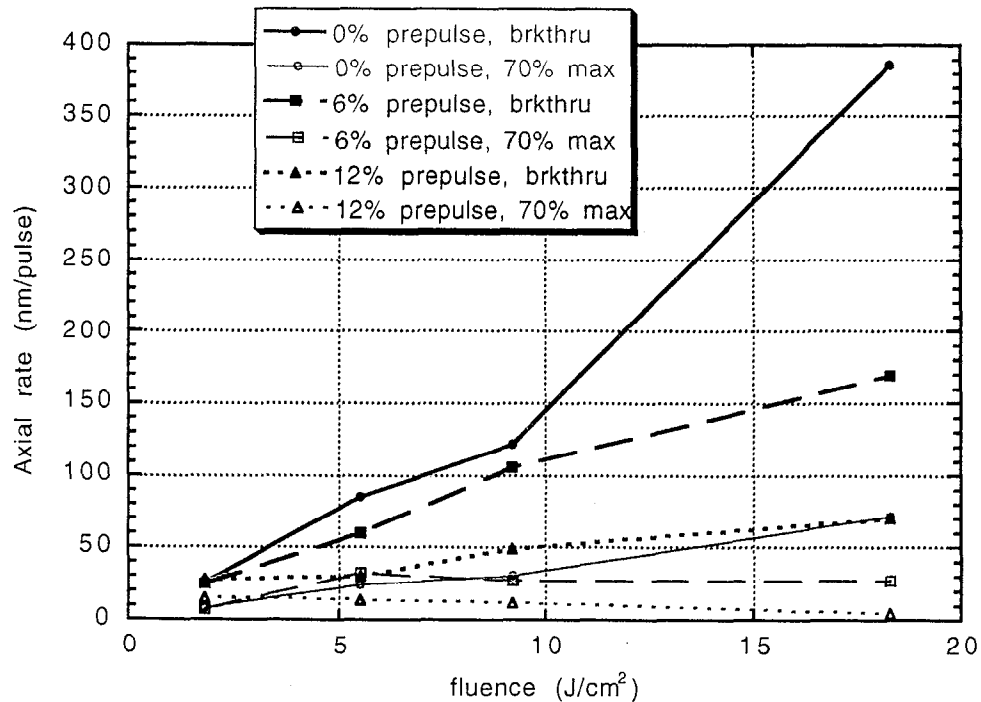
Fig. 4.7(b). Drilling rate through 600 μm thick 316 stainless steel. The prepulse levels are 0% (circles), 6% (squares), and 12% (triangles). Breakthrough rates are the closed symbols (and thicker lines) and transmission rates are the open symbols (and thinner lines). 45° circular polarization.
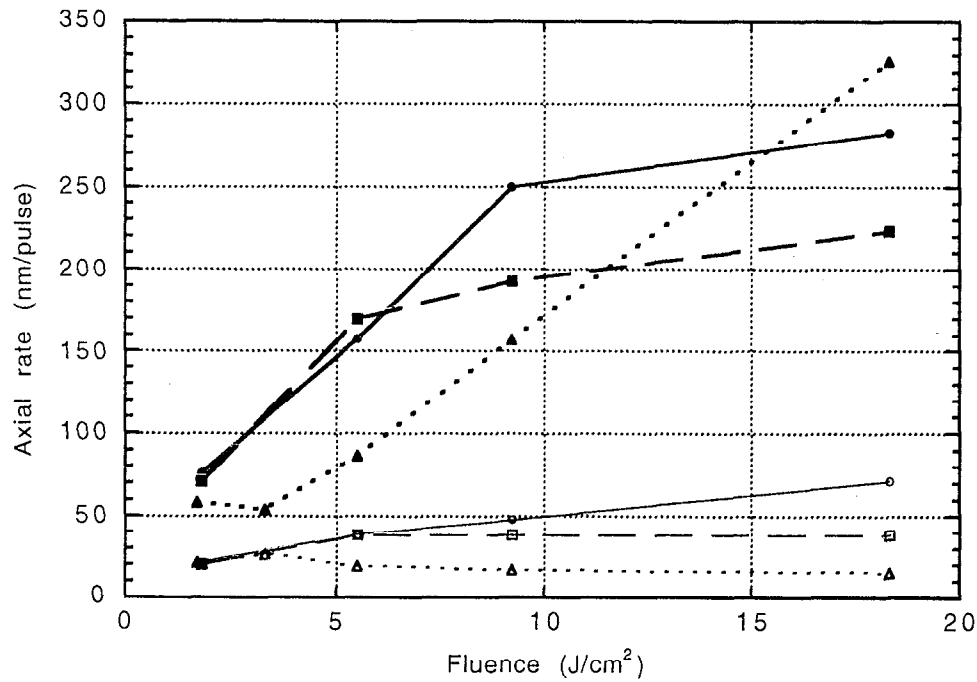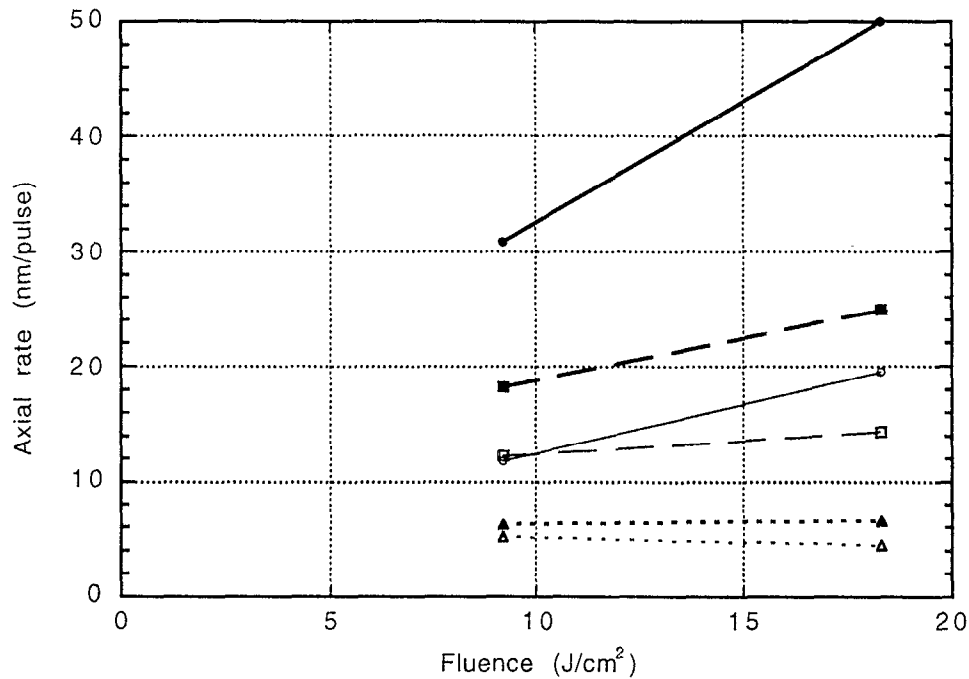
Fig. 4.7(c). Drilling rate through 1200 µm thick 316 stainless steel. The prepulse levels are 0% (circles), 6% (squares), and 12% (triangles). Breakthrough rates are the closed symbols (and thicker lines) and transmission rates are the open symbols (and thinner lines). 45° circular polarization.

We also measured the drilling rates for four different spot sizes: 150 µm, 110 µm, 75 µm, and 55 µm. Figure 4.8 shows the drilling rates determined from breakthrough time (a) and from the time to 70% of maximum transmission (b), for both no prepulse and a 12% prepulse. There are several features of note in these graphs. First, in Fig. 4.8(a) the drilling rate with no prepulse was essentially independent of spot size except for the smallest spot size, 55 µm, which was much slower than the other holes. However, the different hole diameters responded differently in the presence of a prepulse. For the holes drilled with a 110 µm spot, the drilling rate only decreased slightly (the points at 18 J/cm^2 are within the error bars of the measurement), but the rate for holes drilled with a 150 µm spot decreased dramatically. The rate decrease for the two smaller spot sizes was noticeable but smaller. This same behavior was observed to a lesser extent for holes drilled with a 6% prepulse, indicating that the effect is real. Nonetheless, it is not clear what mechanism could be causing this.

54

Fig. 4.8(a). Breakthrough drilling rates for four spot sizes: 150 μm (circles), 110 μm (squares), 75 μm (triangles), and 55 μm (black diamonds). Closed symbols are for no prepulse and open symbols are for a 12%, 120 ps prepulse. 45° circular polarization.
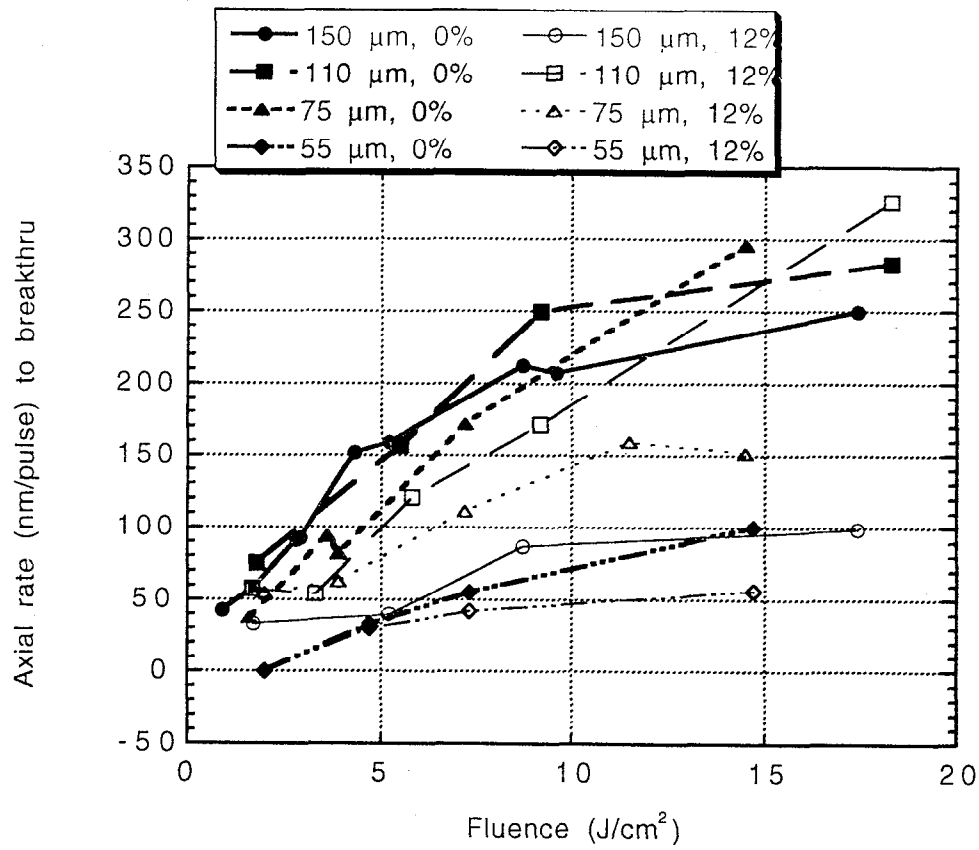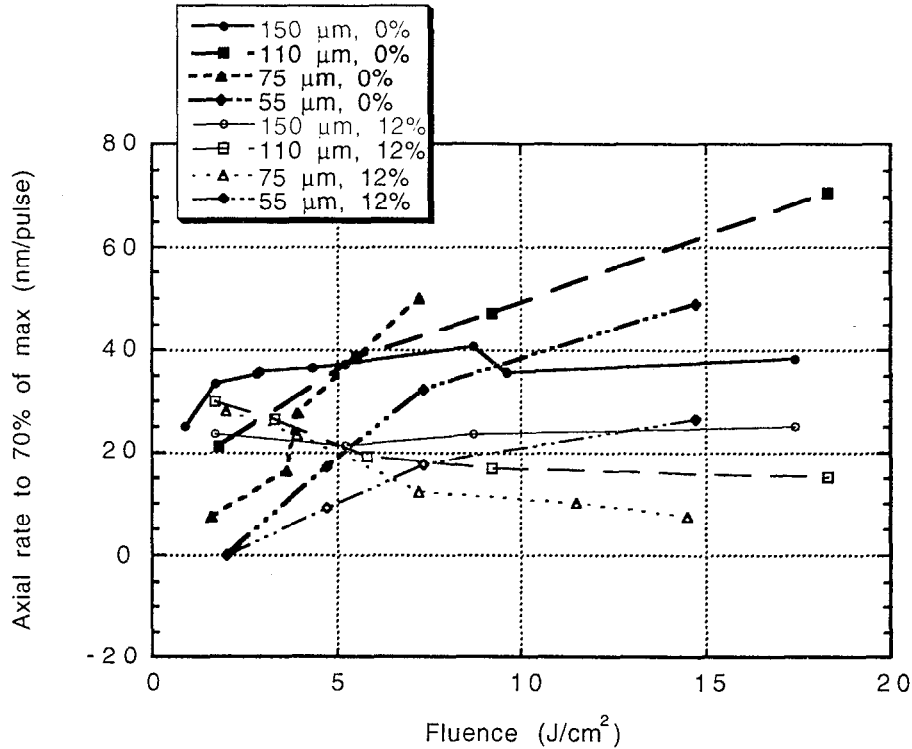
Fig. 4.8(b). 70% transmission drilling rates for four spot sizes: 150 μm (circles), 110 μm (squares), 75 μm (triangles), and 55 μm (black diamonds). Closed symbols are for no prepulse and open symbols are for a 12%, 120 ps prepulse. 45° circular polarization.

In contrast, the rates measured using the 70% of maximum transmission criterion shown in Fig. 4.8(b) exhibited markedly different behavior. For low fluence, the rates decreased monotonically with decreasing spot size. However, the slopes were quite different, with the 150-μm rate becoming lower than the rest at high fluence. When the 12% prepulse was added, the rates for the 110 μm and 75 μm holes decreased dramatically with increasing fluence, as well as being higher for low fluence than the case with no prepulse. This latter fact may be due in part to the fact that the presence of a prepulse has a steeper rising edge on the transmission measurement.

The drilling rate as a function of relative prepulse level is shown in Figs. 4.9–4.11 for the several spot sizes at 10 J/cm² (Figs. 4.9(a), 4.10(a), and 4.11(a)) and for 20 J/cm² (Figs. 4.9(b), 4.10(b), and 4.11(b)). Each is shown for the three thicknesses studied: 300 μm (Fig. 4.9), 600 μm (Fig. 4.10), and 1200 μm (Fig. 4.11). As before, the larger 150-μm diameter hole was most affected by the presence of a prepulse, with the least affected

56
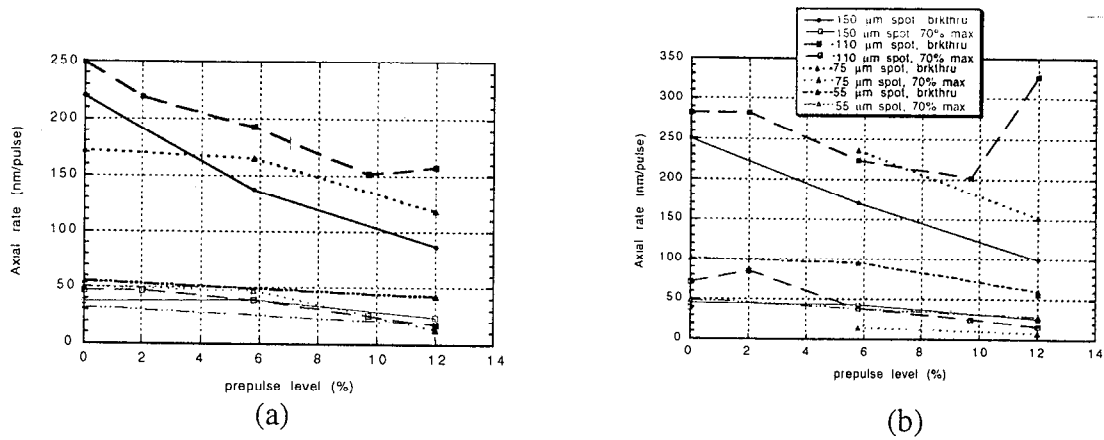
Fig. 4.9. Drilling rate as a function of relative prepulse level for (a) 10 J/cm², and (b) 20 J/cm² in 300 μm thick stainless steel for four spot sizes: 150 μm (circles), 110 μm (squares), 75 μm (triangles), and 55 μm (black diamonds). Closed symbols are for breakthrough rate and open symbols are for 70% transmission rate. 45° circular polarization.

Fig. 4.10. Drilling rate as a function of relative prepulse level in 600 μm thick stainless steel for (a) 10 J/cm² and for three spot sizes: 150 μm (circles), 110 μm (squares), and 75 μm (triangles), and for (b) 20 J/cm² and two spot sizes: 110 μm (circles) and 75 μm (squares). Closed symbols are for breakthrough rate and open symbols are for 70% transmission rate. 45° circular polarization.
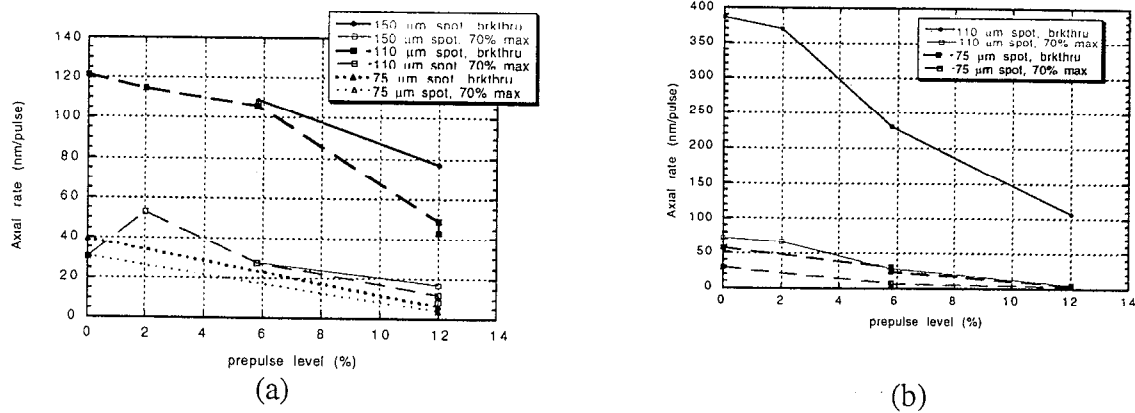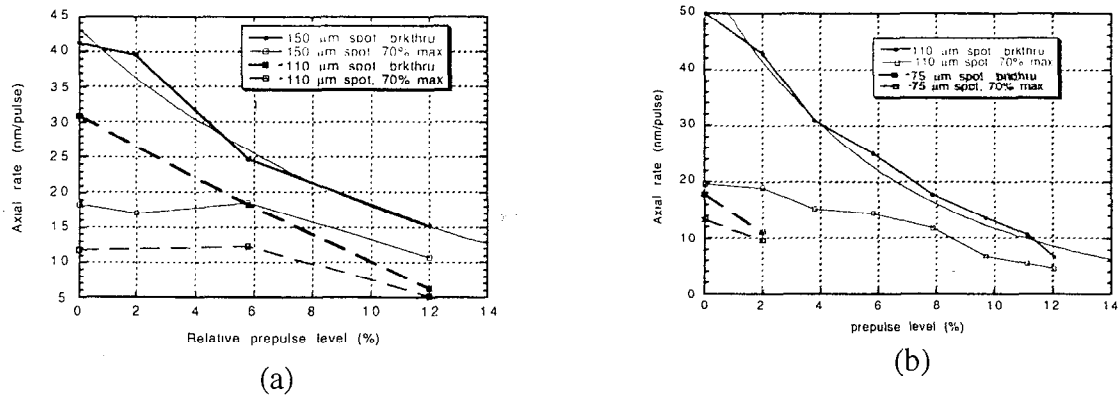
Fig. 4.11. Drilling rate as a function of relative prepulse level in 1200 μm thick stainless steel for (a) 10 J/cm² and for three spot sizes: 150 μm (circles), 110 μm (squares), and 75 μm (triangles) and for (b) 20 J/cm² and two spot sizes: 110 μm (circles) and 75 μm (squares). Closed symbols are for breakthrough rate and open symbols are for 70% transmission rate. 45° circular polarization.

hole size being the 110 μm hole. For this spot size, the rate actually increased dramatically from 9% to 12%. This occurred consistently over many holes. The other curious feature of Fig. 4.9(b) is that the rates for the 75 μm holes as measured by the 0.7 T_{max} criterion were much less than the other three hole sizes. The significance of this is unknown. For the thicker material, the rates decreased consistently with decreasing spot size, with the rates for the larger spot sizes decreasing approximately exponentially for the 1200-μm thick material (see the exponential fits in Fig. 4.11).

We also rotated the 1200-μm thick sample so that the beam impinged at normal incidence and measured the rates with the average power adjusted so that the fluence on the part was still 20 J/cm². We found that the rate for no prepulse was identical to the case of 45° AOI, 50 nm/pulse measured by breakthrough and 20 nm/pulse measured by 0.7 T_{max}, even though the hole length was 30% less and the hole area was 30% smaller. However, the rate decreased more gradually as the level of prepulse was increased than the corresponding case at 45° with the rate being 20 nm/pulse vs. 7 nm/pulse for a 12% prepulse 120 ps in front of the main pulse. This is most likely due to the decreased hole length since the decrease in rate with prepulse is highly dependent on the thickness of the material.

Although we focused mainly on drilling rates in the discussion to this point, it is equally important to realize that the hole quality can be significantly affected by the presence

of a prepulse. Fig. 4.12 shows extreme cases for illustration of how even the entrance morphology can be affected. Fig. 4.12(a) shows a SEM photomicrograph of a round hole drilled with no prepulse while Fig. 4.12(b) shows a hole drilled under similar conditions, but with a significant prepulse approximately 700 ps in front of the main pulse. The prepulse present in Fig. 4.12(b) was the result of slight misalignment of a Pockel's cell in the regenerative amplifier, with the prepulse energy being approximately 50% that of the main pulse. The hole in Fig. 4.12(a) was drilled in approximately 30 s while drill time for the hole in Fig. 4.12(b) was 300 s with no evidence of breakthrough. In fact, there is no observable evidence of a hole in this case.
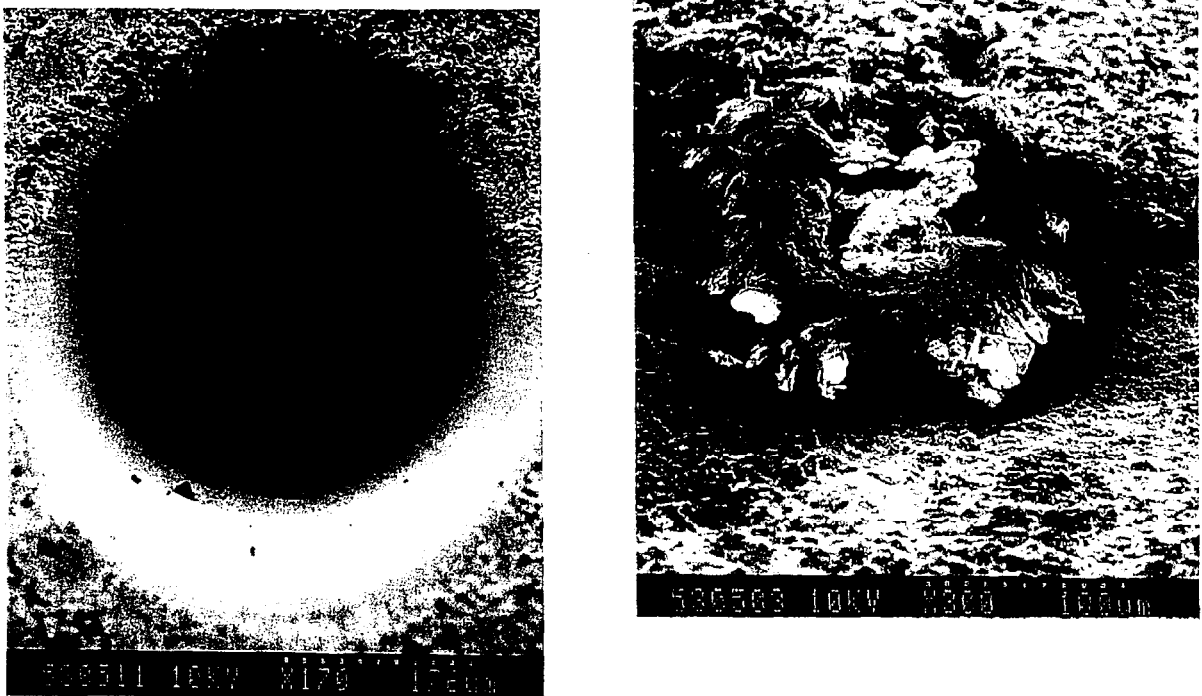
Fig. 4.12. (a) Hole drilled with no prepulse. (b) Hole drilled with 50% prepulse 700 ps before main pulse.

Although the pictures presented in Fig. 4.12 are dramatic, the most common effect on morphology of the presence of a prepulse was manifest in the shape of the exit hole. In most practical cases, the hole broke through and reached its steady-state transmission value. However, the exit hole shape could be dramatically affected as shown in Fig. 4.13. We observed that in the presence of a prepulse, the laser broke through the material in several points, which were often separated by distances larger than the entrance hole diameter.

Fig. 13. Photomicrographs of exit holes with (a) no prepulse and (b) 12% prepulse .

In conclusion, we have demonstrated that the existence of a prepulse in the laser pulse train will deleteriously impact short pulse laser machining results. It not only will slow down drilling rates, but it will also affect the shape of the feature being machined in an adverse way. We find no evidence of any resonance absorption effect proving beneficial for large scale machining. Our results show that with CPA systems employing regenerative amplifiers, particular care must be taken to eliminate to any extent possible any prepulses within the range of ~1 ps to 10–20 ns.

5. Plasma Plume

The plasma plume produced by short-pulse laser ablation is either useful as a diagnostic of the machining process, is a nuisance that coats the laser entrance window to the vacuum chamber, or is extremely beneficial in providing a clean plasma source for thin-film deposition [10].

5.1 Plasma Diagnostics

Two sets of diagnostics were set up to measure the expansion of the plasma away from the ablated surface: an interferometer to measure on short time scales (<10 ns) and a gated imager for longer times (> 2 ns).

5.1.1. Interferometer

A simple experiment was set up to view the plasma coming off the surface of a graphite rod, and then potentially the plasma coming off of other materials. A chamber was set up so that a graphite rod could be suspended in the center and rotated and translated so that it could be ablated without drilling a hole into its surface. The laser beam was split before it was focused on the surface of the graphite rod. A wedge was used to take off approximately 6% of the light, which was then run through a separate optical path. This path took the light in a manner so that it had a slightly longer distance to travel than the beam used to ablate the surface. This probe beam was passed through the plasma plume, then run into Michelson interferometer. The interference pattern was used to image the plume onto a CCD camera chip. The delay between the ablation and probe beam was varied. This experiment worked, but due to problems with the feed-through system and optical design (not enough magnification on the probe) the results achieved were not capable of being analyzed for further study. Future work should use a smaller chamber so that the initial lens of the telescope used for imaging the probe is of shorter focal length. The magnification we used was approximately 4X: a 20 cm lens and a 75-80 cm lens. Even a factor of two increase in magnification would have made a large difference in the quality of the interferometric images produced.

5.1.2. Gated imager

A fast gated imager (gate time 2 ns) was set up to pictorially measure the expansion of the plasma plume away from the surface (Fig. 5.1). Information on the plume expansion velocity (and thus temperature) will be useful in understanding both the initial ablation on a clean surface and ablation deep inside a hole or channel. We were also prepared to incorporate the gated camera with an imaging spectrometer to temporally resolve the spectroscopic emission of the expanding plume. Unfortunately, the project ended before we could obtain any meaningful data from these instruments.
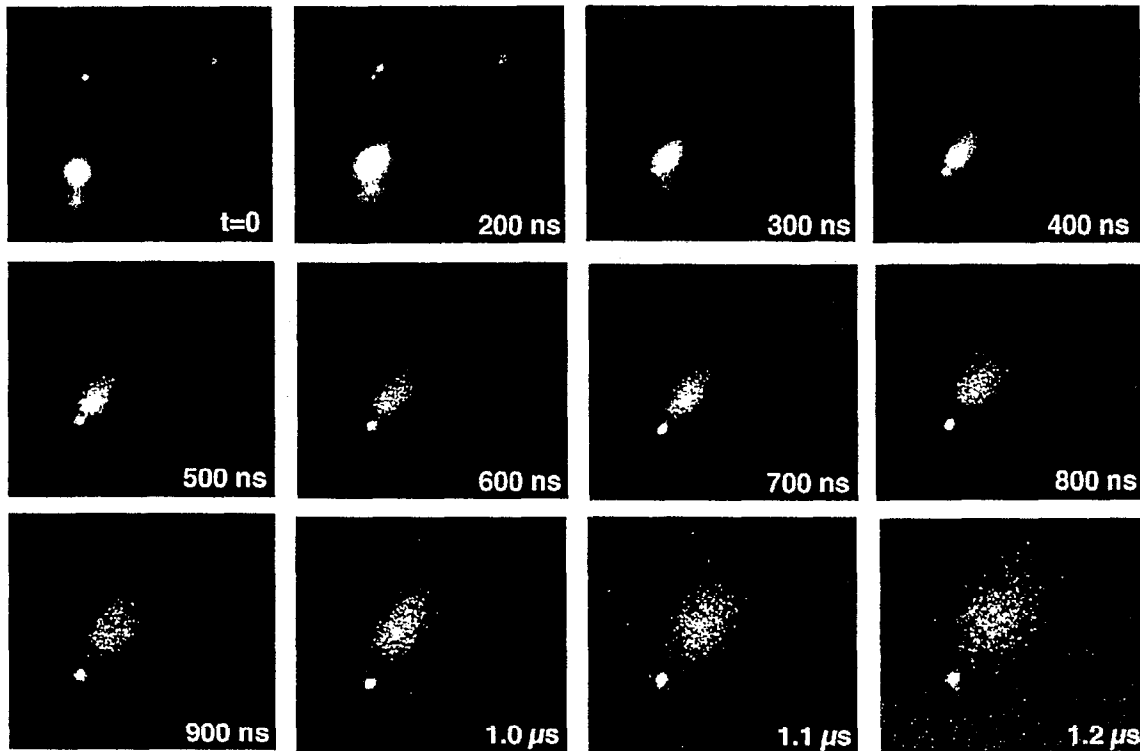
Figure 5.1 Expansion of plasma plume away from the surface of stainless steel. The spatial scale was not calibrated.

5.2 Debris management at entrance window to vacuum chamber

Most of our machining of thick (>300 μm) parts or making high-aspect ratio cuts is done in vacuum to eliminate breakdown of air (or other buffer gas) near the laser focus. Conditions under which high-quality cuts can be made without vacuum are still under investigation, so for now we must deal with the problem of the ablation plume coating the laser entrance window. The first solution is to place a rotating debris shield in the laser path

to block the entrance window. This was shown to work well, however for high material removal rates the debris shield became coated. A 10-cm diameter debris shield was found to last approximately 30 minutes while machining metal with an average laser power of 10 W. At that time the transmission dropped to the 90-93% range and adversely affected the cut quality and rate. If left unchecked, coating of the debris shield eventually runs away, as cutting with poor beam cut quality throws off even more material. We investigated both electrostatic plates and a gas baffle to solve the debris problem.

5.2.1. Electrostatic plates

In a metal-cutting application that required high vacuum ($<$ 1 Torr), we employed two electrostatic plates to deflect the plasma before it coated out on the debris shield. The plates were placed above and below the laser/debris path and were held at +5kV and −5kV. The plates were separated by 1 cm and were located approximately 8 cm from the part and 2 cm in front of the debris shield (Fig. 5.2). By using the biased plates, we achieved a reduction in coating of the debris shield by a factor of ≈20. It was somewhat surprising that the electrostatic plates worked as well as they did, because it was thought that the plasma would have recombined and that the debris would have been neutral at the location of the plates.
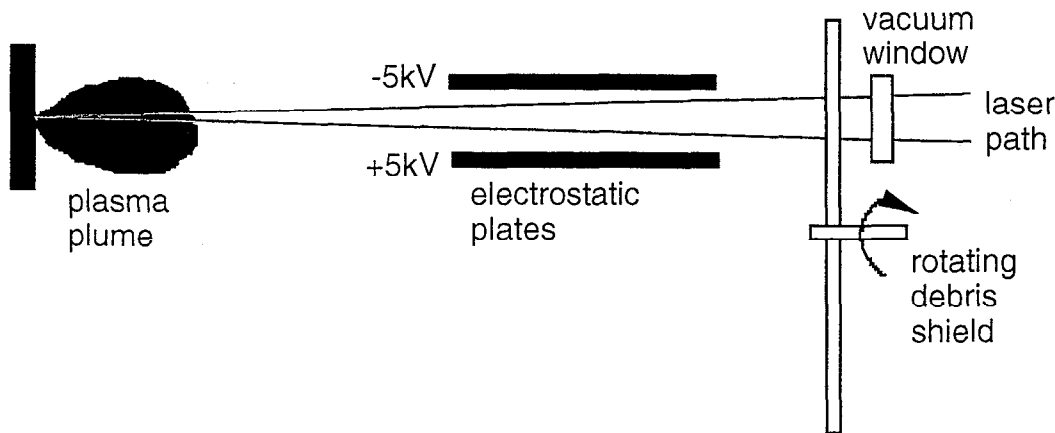

Fig. 5.2. Implementation of electrostatic plates reduced coating of the debris shield by a factor of ≈20.

5.2.2. Gas baffle

For applications where a small gas pressure is acceptable and high voltage is undesirable, a gas baffle works very well in keeping debris off of the entrance window. A set of baffles was built as shown in Fig. 5.3, where gas was bled in near the laser entrance window and the pump was connected to the chamber. The flow was restricted by a set of ever-decreasing orifices with the final diameter being approximately 3 mm. The pressure was monitored on both sides of the baffles using convectron gauges, and the transmission of the entrance window was measured. If N_2 was used, it was found that for chamber pressures above 15 mTorr, the hole quality began to deteriorate somewhat. This was not the case when Ar was used. In fact, for 600 mTorr input pressure of Ar and 25 mTorr chamber pressure, no change in hole quality was observed and no debris was seen on the input window. Thirty holes were drilled in succession through 1-mm thick steel and we observed no coating on the window (transmission was essentially 100%). With no gas, the transmission would have been less than 50%.
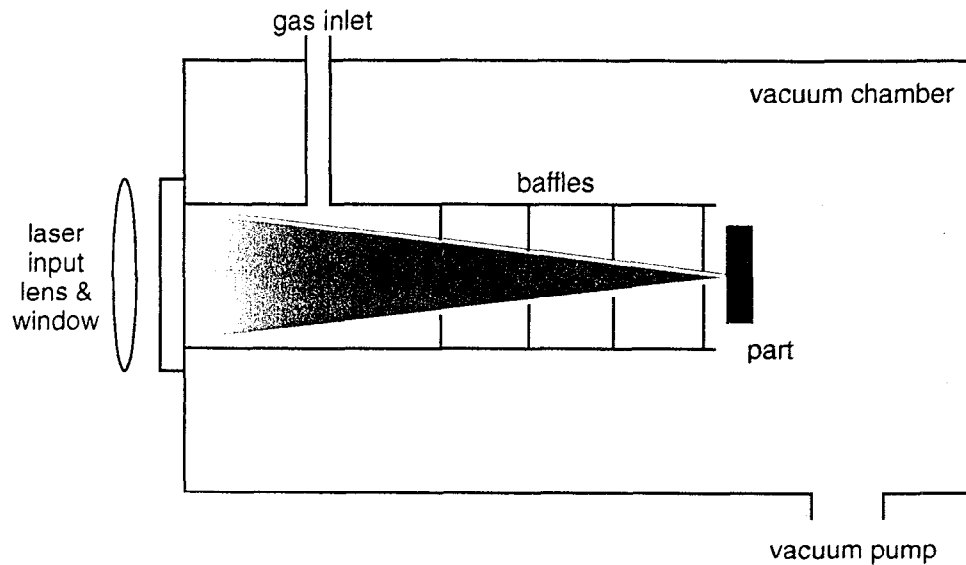

Fig. 5.3 Gas baffles were implemented to keep the laser entrance window clean.

5.3 Deposition of superconducting thin films

Superconducting films were deposited using the Ti:Sapphire laser system in an effort to compare the results with films made at Iowa State University with a 248-nm KrF excimer laser. The superconducting film was a YBaCuO material. The only necessary modification to the experiment was the addition of a system to supply a partial pressure of oxygen to the chamber where deposition is taking place. It was necessary to anneal the films after deposition at room temperature. The films were annealed at 450° C for 3 hrs in an oxygen atmosphere. These films are being tested at Argonne National Laboratory in Chicago for critical temperature and critical current, along with x-ray diffraction. The following table lists the samples chosen for testing:

Sample Number	Distance between target and substrate Cm	Energy mJ/Pulse	Ambient mTorr	Time of deposition mins	Thickness of deposition $\approx$ $^\circ$A
1fs	2	0.5	30	2	4000
2fs	1	2	30	4	12000
3fs	2	2	30	4	17000
4fs	4	1	35	8	8000
5fs	4	1	20	8	12000
6fs	2.5	2	Vacuum	8	8000-17000

6. Machining of non-metals

A couple of interesting applications of short-pulse materials processing on non-metals that we looked at were machining of diamond/graphite and cutting of fiber composites.

6.1 Machining of diamond and graphite

We investigated hole drilling in CVD-grown diamond, single crystal diamond, and highly oriented pyrolitic graphite (HOPG). Ablation threshold measurements were taken on CVD diamond and HOPG. Holes were drilled in all three substances over a range of energy fluences. Extensive experiments were conducted on the HOPG to look at the effects of energy density and pulse width changes on the structure of the surfaces on the material. Characterization was performed using SEM and optical microscopy, and FT-IR microscopy. Further characterization using micro-Raman will be performed along with the possibility of using STM (scanning tunneling microscopy). The results of this work will then be compared with work performed at Iowa State University on modeling and to experimental results from the University of Arkansas, where they are using a 248-nm, 380-fs excimer-dye system.

6.2 Machining of carbon composites

Composite materials are notoriously difficult to machine by conventional laser technology due to the presence (in most cases) of fibers (carbon, glass) and an epoxy or binder that have very different melting temperatures. This can lead to preferential ablation and melting, or thermal loading that causes the layers to separate. Using 150-fs pulses at a relatively high fluence of 100 J/cm^2, we were able to make precise cuts in a 2-mm thick carbon fiber/epoxy matrix (IM7 carbon fiber, 8551-7 toughened epoxy matrix, $[45/90/-45/0]_{2s}$). The cutting rate was 4 mm/min at 1.5 W average laser power. Cuts at lower

fluence did not completely break through at this feed rate. Photographs of the entrance and exit of the cut are shown in Fig. 6.1.
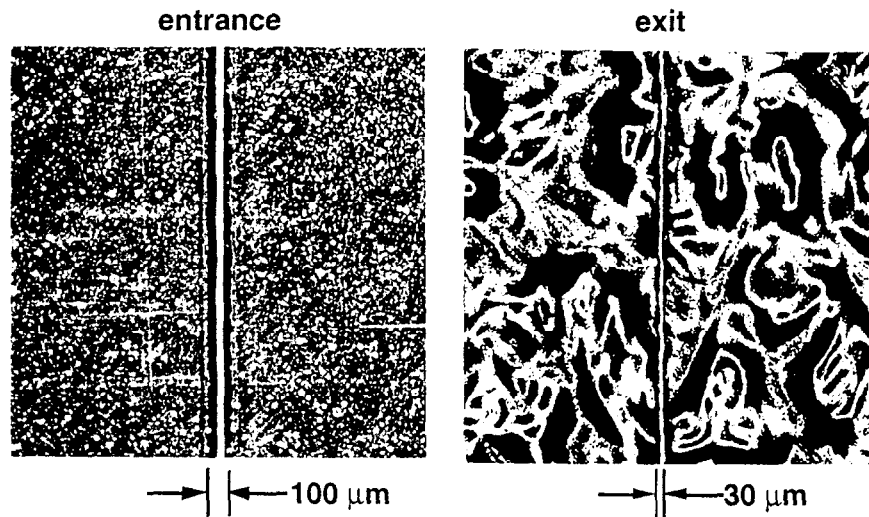

Fig. 6.1 Entrance and exit of short-pulse laser cut in carbon fiber composite. The sample is textured on the exit side, giving the strange pattern.

7. Summary

Short-pulse laser materials processing offers a unique opportunity for machining of nearly any substance with extremely high precision and minimal collateral damage. However, there is still much we do not understand from the scientific viewpoint on the physics and scaling of the material removal.

In Section 2, we formulated a vector optical propagation scheme accounting for laser beam polarization and angle of incidence. This scheme was implemented into the one-dimensional radiation-hydrodynamic code HYADES and permited a self-consistent description of laser absorption and reflection from an expanding plasma. This is important for quantitative modeling since laser pulse absorption can be quite different from that expected from the "cold" Fresnel coefficients. We also developed theoretical estimates of ultimate material removal due to ablation. Detailed calculations demonstrated the high energy efficiency of material removal using ultrashort laser pulses and aided in determining optimal operational parameters.

Section 3 showed us many interesting aspects of the progression of hole drilling as a function of the laser fluence, polarization, and repetition rate. Although the final holes can be made to be clean and round, either the intermediate steps or machining under the wrong conditions can produce some very wild-looking structures.

We showed in Section 4 that the level and timing of any prepulses before the main machining pulse are very important in obtaining clean holes and optimal machining rates. If the level of prepulse is too high and at the wrong location in time (0.5-1 ns), drilling will actually stop. The results of this section have important implications in the design of new and higher power short-pulse laser machining systems.

The plasma plume produced during short-pulse laser ablation is either useful or detrimental. We showed (Section 5) that either electrostatic plates or a gas baffle will greatly reduce coating of the laser entrance window (into vacuum chamber) by the plasma plume. On the other hand, the plume can be used as a diagnostic of the cutting process, and also as an extremely clean source for pulse laser deposition [10]. In section 6, we concluded with a look at machining of diamond, graphite, and carbon/epoxy composities.

During this last year, we made excellent progress in addressing some of the fundamental scientific issues of short-pulse laser materials processing. New diagnostics were readied for further measurements and our modeling code was being upgraded to handle two-dimensional calculations (essential in drilling below surface layer). We saw many new and interesting phenomena that raised further questions in our understanding of the physical processes involved in short-pulse laser material removal. Unfortunately, we were not able to continue this research.

8. References

1. M.D. Perry, B.C. Stuart, P.S. Banks, M.D. Feit, V. Yanovsky, and A.M. Rubenchik, "Ultrashort-Pulse Laser Machining of Dielectric Materials", (20 September 1998), App. Phys. (in press).

2. M.D. Feit, B.C. Stuart, L.B. daSilva, M.D. Perry, A.M. Rubenchik, J. Neev, "Ultrashort laser pulse ablation of hard tissue," M.D. Feit, B.C. Stuart, L.B. daSilva, M.D. Perry, A.M. Rubenchik, J. Neev, OSA Trends in Optics and Photonics **17**, 173-83 (1998).

3. J.P. Armstrong, P.S. Banks, M.D. Feit, R.S. Lee, M.D. Perry, F. Roeske, B.C. Stuart, "Laser cutting of pressed explosives," UCRL-JC-128373, Energetic materials production, processing and characterization, 1998.

4. B.C. Stuart, M.D. Perry, M.D. Feit, L.B. Da Silva, A.M. Rubenchik, J. Neev, "Machining of biological materials, dielectrics, and metals with femtosecond lasers", OSA Trends in Optics and Photonics Vol. 9, Lasers and Optics for Manufacturing, Andrew C. Tam, ed. (Optical Society of America, Washington D.C. 1997), pp. 94-98.

5. B.C. Stuart, M.D. Feit, A.M. Rubenchik, B.W. Shore, and M.D. Perry, "Laser-Induced Damage in Dielectrics with Nanosecond to Subpicosecond Pulses", Phys. Rev. Lett. **74**, 2248-2250 (1995).

6. B.C. Stuart, M.D. Feit, S. Herman, A.M. Rubenchik, B.W. Shore, and M.D. Perry, "Optical Ablation by high-power short-pulse lasers", J. Opt. Soc. Am. B **13**, 459-468 (1996).

7. B.C. Stuart, M.D. Feit, S. Herman, A.M. Rubenchik, B.W. Shore, and M.D. Perry, "Nanosecond to femtosecond laser-induced breakdown in dielectrics", Phys. Rev. B **53**, 1749-1761 (1996).

8. We have modified and extended the HYADES radiation hydrodynamics code developed orignially by J.T. Larsen, and described in *Radiative Properties of Hot Dense Matter,* World Scientific, Singapore (1991).

9. S.A.Akhmanov, V.I Emel'yanov,N.I.Koroteev,V.N.Seminogov, "Effect of powerful laser irradiation on surface of metals and dielectrics: nonlinear-optical effects and nonlinear-optical diagnostics", Usp.Fiz. Nauk 147,675.1985 [Sov.Phys.Usp.26.1084.1985]

10. P. S. Banks, B. C. Stuart, L. Dinh, M. D. Feit, A. M. Rubenchik, W. McLean, M. D. Perry, "Short Pulse Laser Production of Diamond Thin Films", UCRL-XXXXXX, 1998.